

## **General Disclaimer**

### **One or more of the Following Statements may affect this Document**

- This document has been reproduced from the best copy furnished by the organizational source. It is being released in the interest of making available as much information as possible.
- This document may contain data, which exceeds the sheet parameters. It was furnished in this condition by the organizational source and is the best copy available.
- This document may contain tone-on-tone or color graphs, charts and/or pictures, which have been reproduced in black and white.
- This document is paginated as submitted by the original source.
- Portions of this document are not fully legible due to the historical nature of some of the material. However, it is the best reproduction available from the original submission.



# 2.5 kW ADVANCED TECHNOLOGY ION THRUSTER

## FINAL REPORT

(NASA-CR-135076) THE 2.5 kW ADVANCED  
TECHNOLOGY ION THRUSTER Final Report, 13  
Jun. 1974 - 29 Feb. 1976 (Hughes Research  
Labs.) 106 p HC \$5.50

CSCI 21C

N76-33283

G3/20 Unclass 07185

BY

ION PHYSICS DEPARTMENT STAFF  
HUGHES RESEARCH LABORATORIES  
A DIVISION OF HUGHES AIRCRAFT COMPANY

3011 MALIBU CANYON ROAD  
MALIBU, CALIFORNIA 90265



PREPARED FOR  
NATIONAL AERONAUTICS AND SPACE ADMINISTRATION  
NASA LEWIS RESEARCH CENTER

CONTRACT NAS 3-17831

ROBERT T. BECHTEL, PROGRAM MANAGER

1. Report No. NASA CR-135076	2. Government Accession No.	3. Recipient's Catalog No.	
4. Title and Subtitle  2.5 kW ADVANCED TECHNOLOGY ION THRUSTERS		5. Report Date April 1976	
		6. Performing Organization Code	
7. Author(s)  R.L. Poeschel, et al.		8. Performing Organization Report No.	
9. Performing Organization Name and Address  Hughes Research Laboratories 3011 Malibu Canyon Road Malibu, CA 90265		10. Work Unit No.  YOS 5215	
		11. Contract or Grant No.  NAS 3-17831	
12. Sponsoring Agency Name and Address National Aeronautics and Space Administration Lewis Research Center 21000 Brookpark Road Cleveland, OH 44135		13. Type of Report and Period Covered  13 Jun 1974 - 29 Feb 1976	
		14. Sponsoring Agency Code	
15. Supplementary Notes  Project Manager: Robert T. Bechtel NASA Lewis Research Center, Cleveland, Ohio			
16. Abstract  The program reported on here has been concerned with establishing some of the capabilities and limitations of the 700/800 series 30 cm Engineering Model Thruster Design as specified under the Low Voltage Thruster Program (NAS 3-16528) and thereby to establish a base line for future advanced technology. The work is a continuation of that begun under the 2.5 kW Advanced Technology Ion Thruster Program (NAS 3-16949). A representative thruster has been extensively documented with respect to performance parameters and characteristics at selected ion beam currents in the 0.5 to 2.75 A range, including measurements of thrust losses resulting from doubly-charged ions and ion beam divergence. Corrected total efficiency is relatively insensitive to operating parameter selection at any given power level, and the relationship between corrected total efficiency and power level agrees well with the maximum propellant analysis of Kaufman.  Factors affecting doubly-charged ionization were studied and it was found that the fraction of doubly-charged ions is directly proportional to the discharge chamber propellant utilization. The parameter that most affects this proportionality is the accel aperture diameter (which controls neutral atom loss).  Thruster-power conditioner interactions were studied with the result that previous power supply specifications remain satisfactory. Options for reducing the number of power supplies required were demonstrated to be feasible.  A study of gimbal actuator designs was conducted with the goal of selecting a particular approach for design and development. The conclusion drawn was that optimum gimbal actuator design depends heavily on the thruster application and consequently the effort was concluded by developing a computer program to aid in specifying the gimbal requirements for the thrust vectoring required in a specific application.			
17. Key Words (Suggested by Author(s)) Electric Propulsion 30 cm Ion Thruster Double Ion Thrust Loss Automatic Controller Mercury Propellant		18. Distribution Statement  UNCLASSIFIED - Unlimited	
19. Security Classif. (of this report) Unclassified	20. Security Classif. (of this page) Unclassified	21. No. of Pages 106	22. Price*

\* For sale by the National Technical Information Service, Springfield, Virginia 22151

## FOREWORD

The work described herein was performed in the Hughes Research Laboratories Ion Physics Department of the Hughes Aircraft Company. This department is managed by Mr. J.H. Molitor. The work was performed under Contract NAS 3-17831, monitored by Mr. Robert T. Bechtel of NASA Lewis Research Center. Major technical contributions to this effort were made by:

R.L. Poeschel	Project Manager and principal investigator
R.P. Vahrenkamp	Thruster documentation and double ionization studies
S. Hansen, B. Herron and C. Collett	Thruster-power processor interaction
J. W. Ward	Data analysis
S. Kami, J.W. Ward, and T. Masek	Gimbal system study
L. Dulmage, and R. Scholl	Data collection, instrumentation, and technical assistance

PRECEDING PAGE BLANK NOT FILMED



## TABLE OF CONTENTS

SECTION		PAGE
	SUMMARY . . . . .	13
I	INTRODUCTION . . . . .	15
II	DOCUMENTATION OF 30 cm THRUSTER PERFORMANCE . . . . .	17
	A. Experimental Procedures . . . . .	17
	B. Experimental Results . . . . .	22
	C. Additional Results . . . . .	36
III	DOUBLY-CHARGED ION INVESTIGATION . . . .	55
	A. Beam Probe and Measurement Technique . . . . .	55
	B. Small Hole Accelerator Grid . . . . .	56
	C. Experimental Results . . . . .	58
IV	THRUSTER POWER CONDITIONER INTERACTIONS . . . . .	69
	A. Discharge Current/Voltage Oscillations . . . . .	69
	B. Beam and Accelerator Power Supply Requirements . . . . .	76
	C. Utilization of Discharge Power Supply for Auxiliary Functions . . . . .	78
V	THRUSTER-GIMBAL SYSTEM ANALYSIS . . . . .	89
	A. Survey of Gimbal Mechanisms for Thrust Vector Control . . . . .	89
	B. Thruster Gimbaling Computer Program . . . . .	92
	C. Analysis . . . . .	95

SECTION	PAGE
VI CONCLUSIONS . . . . .	101
REFERENCES . . . . .	103
APPENDIX . . . . .	105

## LIST OF ILLUSTRATIONS

FIGURE		PAGE
1	Discharge chamber schematic . . . . .	18
2	Schematic diagram of principal thruster power supplies and meter locations for direct measurement of thruster performance parameters . . . . .	20
3	Power/efficiency throttling characteristic for operation at constant discharge loss for 37 V and 39 V discharge voltage . . . . .	26
4	Power/efficiency throttling characteristics for operation at constant discharge voltage and constant discharge losses of 185, 200, and 250 eV/ion . . . . .	26
5	Power/efficiency characteristic for operation at constant discharge loss and discharge voltages of 35 V, 37 V, and 39 V . . . . .	27
6	Comparison of power/efficiency characteristics calculated using Kaufman's maximum propellant efficiency theory with thruster data from this investigation . . . . .	29
7	Schematic drawing of thruster discharge chamber showing thermocouple locations . . . . .	31
8	Comparison of discharge current waveforms for four beam current values . . . . .	34
9	Control characteristics and floating potential variations for neutralizer 806. . . . .	38
10	Variation in characteristic after accumulated time and variation of floating potential with time . . . . .	40
11	Cross section of neutralizer cathode indicating location of thermocouples . . . . .	42
12	Single ion beam divergence at $r = 10.9$ cm for beam currents of 2.0 and 0.5 A . . . . .	45
13	Geometric configuration of collimating probe used to sample angular current density from accel electrode . . . . .	47

# LIST OF ILLUSTRATIONS (Continued)

FIGURE		PAGE
14	Experimental data showing angular current density distribution emanating from holes on beam centerline for different accel voltages . . . . .	48
15	Experimental data showing angular current density distribution emanating from edge holes showing fringe beam ions at high angles . . . . .	49
16	Model used to simulate fringe beam ions which are deflected outward due to the distortion of the virtual ground neutralization plane . . . . .	52
17	Measured current of radially directed Group 4 charge exchange as a function of distance downstream from ground screen electrode for 0 to 90° and 105° . . . . .	53
18	Ion beam trajectories computed for variations in accelerator grid aperture diameter . . . . .	57
19	Performance map data relating the double ion ratio to mass efficiency . . . . .	60
20	Double ion fraction and neutral loss rate as a function of beam current . . . . .	61
21	Double ion fraction as a function of radial current density . . . . .	63
22	Double ion fraction as a function of mass efficiency for selected radial locations . . . . .	65
23	Double ion fraction as a function of mass efficiency for three different accelerator grids . . . . .	67
24	Double ion fraction as a function of total thruster efficiency . . . . .	68
25	Magnetic field plotting apparatus . . . . .	71
26	Variation in axial magnetic field component $B_z$ on the thruster axis with and without magnetic baffle current . . . . .	72

# LIST OF ILLUSTRATIONS (Continued)

FIGURE		PAGE
27	Variation in radial magnetic field along a radius in the plane of the baffle, with and without magnetic baffle current . . . . .	72
28	Axial magnetic field variation on the discharge axis near the cathode orifice with magnetic baffle current as a parameter . . . . .	73
29	Illustration showing effect of magnetic baffle control current on the field distribution within the cathode polepiece . . . . .	75
30	Shared discharge supply wiring diagram . . . . .	80
31	JPL gimbaling concept . . . . .	86
32	Rockwell linear actuator gimbaling concept. . . . .	88
33	Boeing tape drive gimbaling concept . . . . .	91
34	Conventional tape drive gimbaling concept . . . . .	91
35	Coordinate system used for thrust and torque calculations . . . . .	93
36	Computer printout for thruster gimbaling computer program . . . . .	93
37	Coordinate system used for thrust and torque calculations . . . . .	96

# LIST OF TABLES

TABLE		PAGE
I	Engineering Model Thruster Performance Data . . . . .	25
II	Engineering Model Thruster Thermal Data . . . . .	32
III	Neutralizer Temperature Variation, $I_B = 2.0$ A . . . . .	44
IV	Variation of Accel Aperture Diameter Across Grid S/N 644 . . . . .	46
V	Performance Parameters for Optics S/N 650 and S/N 644 . . . . .	50
VI	Parameters for Low Transmission Accelerator Grid Ion Optical System Design . . . . .	58
VII	Shared Discharge Supply Control Functions . . . . .	81
VIII	Heater Relay Logic States . . . . .	82
IX	Summary of Estimated Failure Rates and Weights for Different Thruster Gimbal Systems . . . . .	94

PRECEDING PAGE BLANK NOT FILMED



## SUMMARY

The 2-1/2 kW Advanced Technology Ion Thruster Program documented in this report was performed with the goal of establishing the technology capabilities and limitations of the 30 cm ion thruster design that was representative of the best available technology at the time the work was performed (the 700/800 series Engineering Model Thruster Design). The information obtained here has been and should continue to be useful in determining future technology requirements and for assessing 30 cm thruster capabilities in planning the application of ion thrusters for prime propulsion. Data was obtained to show the performance characteristics (efficiencies, thermal data, stability, etc.) for a variety of operational parameters in the 0.5 A to 2.75 A beam current range. These data show that the maximum thruster efficiency that can be obtained at any given power level is not critically dependent on parameter selection when the effect of beam divergence and doubly-charged ions is accounted for. Although the data obtained was for a single thruster, the observed effects and trends in parameter variation reported here should have general applicability. Relatively stable and repeatable operation was demonstrated for this thruster in the 0.5 A to 3.0 A range of beam currents without any indication of thermal or control problems.

Double ionization in the discharge chamber was investigated primarily as a thrust loss factor but also because the doubly-charged ions are thought to be responsible for discharge chamber erosion. Discharge parameters such as discharge voltage, discharge power and propellant flow split (magnetic baffle current) were varied with the net result being that there appears to be a fundamental relation between propellant utilization efficiency and the fraction of doubly-charged ions measured in the beam for a given thruster (dimensional specification). A relatively substantial body of data were collected in support of this supposition. The dimensional parameter that most affects the relationship between double ionization and propellant utilization is found to be the ion optics accelerator grid aperture size (which governs

the loss of neutral atoms from the discharge chamber). Examination of this effect under this program has only begun to explore this parameter as a possibility for reducing double ionization. Double ionization is considered the largest obstacle to achieving higher thruster efficiency and/or longer lifetime based on the results of this investigation.

Investigation of thruster-power conditioning interactions showed that the 700/800 series Engineering Model Thruster differs little from the earlier designs insofar as loss of stable control power conditioning requirements and interactions are concerned. Discharge current or voltage oscillations are observed in the 10 to 20 kHz range during typical operations, but these oscillations cannot be related to any detrimental thruster behavior. Options for reducing power supply requirements and complexity were studied with the net result being that the beam (screen) and accelerator power supplies could be combined, and the discharge power supply could be controlled to satisfy the preheat and low voltage cathode keeper functions, thereby eliminating the requirements for these power supplies. Employing the discharge power supply in this manner would also make more power available for preheat and thereby shorten the thruster start-up time.

A study was conducted to determine whether generally applicable thruster gimbal actuators could be identified that would meet most application requirements and present some advantage over other choices. The results of this study showed that the gimbal requirements vary widely with respect to the application being considered, and there is no well defined "optimum" choice of actuator that could satisfy this wide range of requirements. Consequently, in place of attempting an "optimum" design, a computer analysis was developed to aid in determining gimbal actuator requirements to meet specified thrust vectoring and thruster array parameters.

## I. INTRODUCTION

The work described in this report was performed under the 2-1/2 kW Advanced Technology Ion Thruster Program (Contract NAS 3-17831) and is an extension of investigations begun under a prior program (Contract NAS 3-16949). The objective of the program was to establish the performance characteristics and capabilities of the 700/800 series Engineering Model Thruster (EMT) design that was being structurally qualified and endurance tested under other concurrent programs (Contract NAS 3-15523 and NAS 3-17803) and thereby to establish a baseline for future technology. Much of the data generated under this program may be obsolete because of design changes recently incorporated into the 900 series Engineering Model Thruster, however the trends observed are still valid.

The work was performed under four distinct tasks. The first task was that of documenting thruster performance characteristics over a range of operating parameters and power levels. One objective was to find a method for selecting operating parameters so that the thruster efficiency is maximum for each power level within the operating range. A second objective was simply to document the limits of operation and the efficiency parameters necessary for mission analysis. The second task was concerned primarily with identifying parameters which control double ionization processes with the goal of minimizing the production of doubly-charged ions in the discharge. The third task was devoted to investigating power processor-thruster interactions with the goal of identifying modifications to thruster or power processor design that could simplify or improve the interface. The final task was to study gimbal requirements for typical thrust vectoring and to design a prototype gimbal actuator on which development for future needs might be based. Although only this last task is truly independent of the work conducted under the other tasks, this report has been organized in sections that describe the work pertinent to each of these four tasks.

## II. DOCUMENTATION OF 30 CM THRUSTER PERFORMANCE

The performance of an ion thruster is characterized by a number of operational properties. Total overall thruster efficiency has received primary consideration in the development of discharge chamber and ion optical system technology and consequently this parameter has been given most attention. Determination of overall efficiency requires measurements of all electrical parameters, propellant flow rates, and thrust reduction factors necessary to account for contributions to the measured beam current of doubly-charged ions and non-axial ion trajectories which produce less thrust. At the outset, it was considered possible that total efficiency for any given power input could be maximized by judicious selection of controllable operating parameters such as discharge voltage or power, magnetic baffle current, etc. Thus an algorithm for adjusting operating parameters to provide maximum thruster efficiency at any desired power level could be generated. While obtaining thruster efficiency data, a number of other performance parameters were monitored. These parameters included temperatures of cathodes, isolators, and vaporizers, waveforms of the time variations in discharge and beam currents and voltages, and erosion rates on selected discharge chamber surfaces. The thruster was operated over a range of beam currents from 0.5 A to 2.75 A, representing a variation in input power from 0.7 to 3.8 kW.

### A. Experimental Procedures

#### 1. Thruster Design and Test Equipment

The evaluation of thruster performance described here was carried out with a thruster which is representative of the 700/800 series EMT design<sup>1,2</sup> in all important dimensional, electrical, and thermal characteristics. This thruster configuration is shown schematically in Fig. 1, and is identified as Thruster S/N 301-B. The thruster tested differs from the EM design only in the materials

PRECEDING PAGE BLANK NOT FILMED

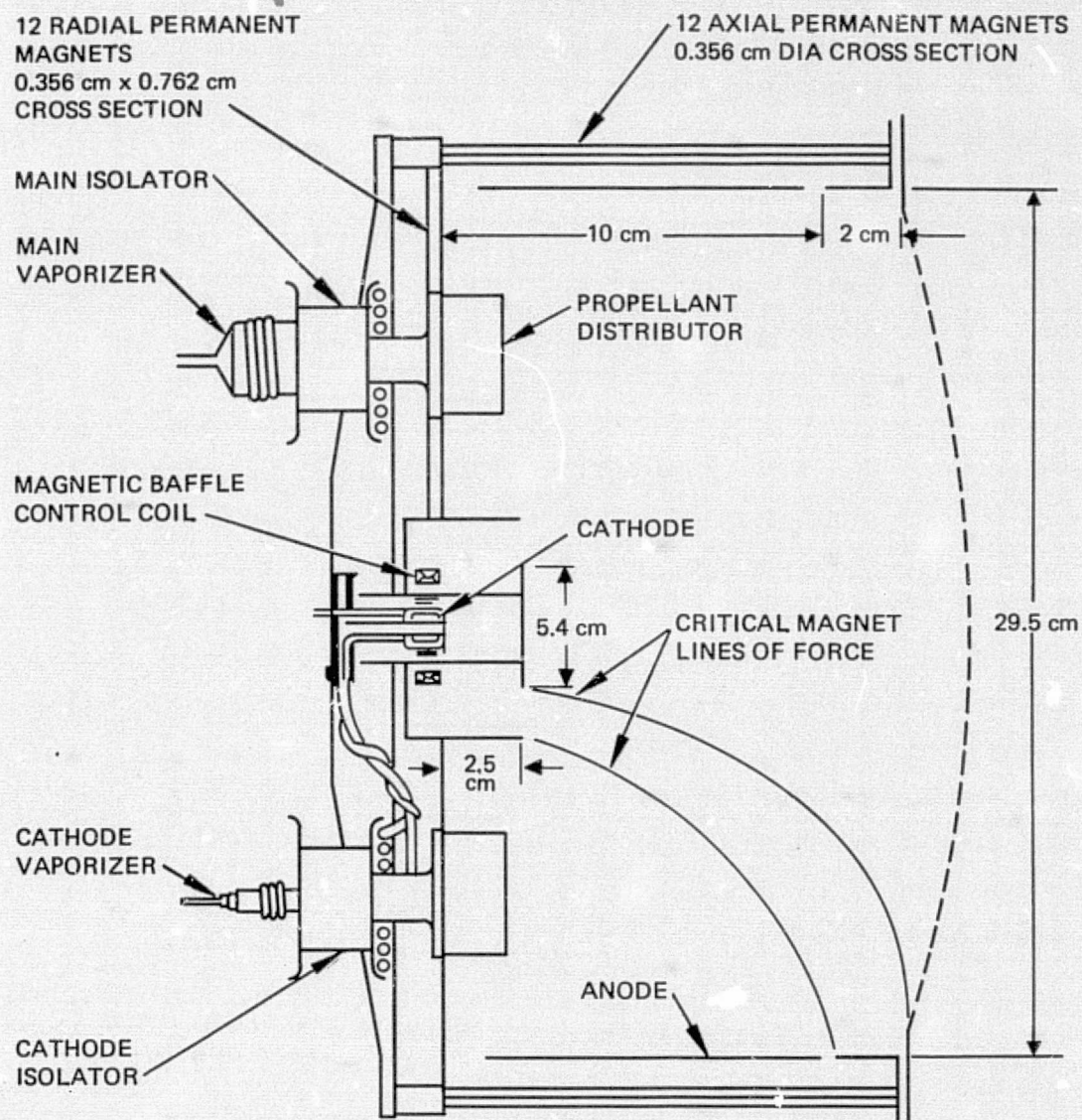


Figure 1. Discharge chamber schematic.

(stainless steel instead of titanium), fabrication techniques (fasteners instead of welds) and structural elements. Testing was performed in a cryopumped vacuum facility, which is 9 ft (2.7 m) in diameter and 18 ft (5.4 m) long and maintains an ambient pressure in the range from 1 to  $5 \times 10^{-6}$  Torr in the vicinity of the thruster during testing. The thruster is operated and controlled using a transistorized power processor<sup>3,4</sup> with principal power supplies and metering connected as shown schematically in Fig. 2. All evaluation was performed with power processor control loops closed, as would be normal in an actual flight application. Each set of operating conditions was maintained for a sufficiently long time period to obtain propellant flow rate data.

## 2. Electrical Measurements

Electrical measurements were of two types: steady state meter readings for power and thrust determination, and oscilloscope recordings of beam and discharge voltage and current waveforms for stability evaluations. Time-varying parameters were monitored only in the dc to 50 MHz range since higher frequencies are not considered important to the operation or control of the thruster system. All metering is calibrated with respect to primary standards, and metered electrical measurements are accurate to within  $\pm 1\%$ .

## 3. Propellant Flow Measurement

Propellant flow rate was measured by recording propellant reservoir content at regular time intervals and by graphically obtaining a "best fit" linear rate to the recorded data. Two methods were used to monitor propellant reservoir content: one measures the volume of mercury in a calibrated glass pipette while the other weighs the mercury stored using load cells calibrated with primary standards. These methods were used interchangeably and produced results which agreed within 1%.





100

#### 4. Correction Factors and Beam Probes

Thrust corrections which account for doubly-charged ions and nonaxial beam trajectories were measured with a collimating mass spectrometer probe. This apparatus measures the singly- and doubly-charged beam current components as a function of angle and grid location along a diameter of the ion extraction system. Data are recorded automatically and analyzed by computer. Assuming azimuthal symmetry, the measured current densities can be integrated and thrust factors are computed for use in correcting the measured beam current so that the thrust can be calculated from beam current and voltage on the basis of a beam of singly-charged paraxially ejected ions. These correction factors are defined as follows:

$$T_a = \alpha F_t T_c, \quad (1)$$

where  $T_c$  is the thrust calculated from measured beam current,  $\alpha$  is the factor which accounts for the reduced thrust produced by doubly-charged ions,  $F_t$  accounts for the thrust reduction on nonaxial or diverging ion velocity components, and  $T_a$  is the actual thrust produced. The thrust determined by using these measured correction factors with metered values of beam current and voltage has been reported to agree to within 1% of the value determined by direct thrust measurements at NASA Lewis Research Center.<sup>5</sup> Another parameter has been defined which relates the ionized mass flow rate  $\dot{m}_i$  to the neutral mass flow rate  $\dot{m}_o$  by

$$\frac{\dot{m}_i}{\dot{m}_o} = \beta \frac{I_B M}{e \dot{m}_o} \quad (2)$$

where  $I_B$  is the beam current,  $\beta$  is the factor which takes into account the doubly-charged ions,  $e$  is the electronic charge, and  $M$  is the mass of a mercury ion. In addition to the ExB separator, a collimated

Faraday cage was also used for the investigation of fringe ions and charge-exchange ions. Since this probe could be positioned to much larger dispersion angles than the ExB assembly, it allowed a more detailed examination of beam divergence characteristics.

#### 5. Temperature Measurements

Thermocouples were attached to thruster components in 12 locations which have critical temperature requirements. Temperatures were monitored at regular time intervals, as in the case of the propellant flow determination in order to make certain that steady-state conditions had been established. It should be emphasized that temperature distributions reported here are accurate only for steady state thruster operation in a large, cryopumped vacuum facility.

#### 6. Erosion Measurements

A number of techniques were attempted to monitor erosion of discharge chamber components by ion sputtering. These included comparison of component photographs between tests, use of small cover plates which had alternating thin layers of different colored metals (iron and copper for example), and cover plates which had been highly polished and then coated with appropriate materials (e.g., tantalum, iron). Only the latter technique using a Dektak profilometer to measure the depth of material removed from a coated slice of polished silicon wafer produced any quantitative information.

### B. Experimental Results

Parameter variation followed a schedule whereby baseline performance conditions were established at each beam current value (0.5 A, 1.0 A, 1.5 A, and 2.0 A) for fixed values of the following parameters:

Beam Voltage, V	1100
Accel Voltage, V	500
Discharge Voltage, V	37
Magnetic Baffle Current, A	3.5

Having obtained all forms of data for this set of parameters, a systematic variation was pursued to determine whether increases in total corrected thruster efficiency could be produced and to document which other parameters might be influenced. The more significant results of these experiments are described in this section.

### 1. Performance Mapping

Since the foremost objective of this parameter variation study was to maximize the total corrected efficiency for thruster operation over a beam current range from 0.5 A to 2.0 A, this aspect of the experimental results will be discussed first. Total corrected thruster efficiency,  $\eta_T$ , is defined here as

$$T = \frac{T_a^2}{2\dot{m}_o P} = \eta_p \eta_u \alpha^2 F_t^2 \quad (3)$$

where

$$\eta_p = \frac{V_B I_B}{P}$$

$$\eta_u = \frac{I_B}{\dot{m}_o}$$

and  $P$  is the total input power,  $V_B$  and  $I_B$  are the metered beam voltage and current, respectively, and the remaining quantities have been defined above. At the outset of this investigation it was considered possible that tradeoffs might exist between the quantities in eq. (3) which could appreciably affect the value of the total efficiency. The performance data which were obtained to establish a basis for selecting optimum parameters are presented as Table I. These data were collected over a number of moderate length testing periods and are

representative of operating points which are consistently reproducible. Higher and lower efficiencies have been obtained with both the thruster used in this study and other thrusters of the EMT design. When all sources of error are considered, the accuracy of the overall corrected efficiency is limited to  $\pm 1\%$ . The data in Table I have been organized for comparison of variations at each beam current level. "Normal" neutralizer parameters have been used in the computation of  $\eta_p$ ,  $\eta_u$ , and  $\eta_T$  because the neutralizer used in these tests was not operating with what are considered "representative" characteristics. One of the first observations to be made regarding the data in Table I is that for any given beam current, there are a number of choices of the controlled parameters for which the variation in  $\eta_T$  is not greater than the absolute accuracy of  $\eta_T$ . Consequently, it appears that  $\eta_T$  is relatively insensitive to the selection of control parameters, and some factor other than  $\eta_T$ , such as minimizing the ratio of doubly-charged ion current to total current, or simplifying of control algorithms could be used to make the parameter selection.

A number of trends or tendencies can be explored by cross-plotting data from Table I. The dependence of  $\eta_T$  on power input, or the throttling characteristic is considered first. Figures 3, 4, and 5 show this "power throttling" characteristic for several combinations of parameters. It is apparent, as stated earlier, that the choice of parameters, or an inadvertent variation of control parameters, does not significantly alter this characteristic. It is interesting to compare actual thruster data with a theoretical throttling characteristic computed on the basis of Kaufman's maximum propellant utilization theory.<sup>6</sup> In brief, this theory states that "the loss rate of un-ionized propellant at the maximum utilization is nearly a constant over a wide range of total propellant flow rate, permitting rapid prediction of total flow rate effects from operation at one total flow rate." Quantitative agreement between thruster data and performance predicted by this theory has not always been good,<sup>5</sup> possibly because the presence of doubly-charged ions has not been adequately taken into account. Similarly, it has also been considered that this theory is invalidated by the flexibility in

Table I. Engineering Model Thruster Performance Data

Controlled Parameters							Measured Thruster Parameters							Beam Diagnostics				Total Efficiency Factor $\eta_F^c$
Beam Current, A	Beam Voltage, V	Accelerator Voltage, V	Discharge Current, A	Discharge Voltage, V	Magnetic Baffle Current, A	Discharge Chamber, eV/ion	Total <sup>b</sup> Power Input, W	Total <sup>b</sup> Corrected Efficiency, $\eta_p$ , %	Power <sup>b</sup> Efficiency, $\eta_{pe}$ , %	Propellant Utilization Efficiency, $\eta_u$ , %	Main Vaporizer Propellant Flow Rate, A (Equivalent)	Cathode Vaporizer Propellant Flow Rate, A (Equivalent)	Total <sup>b</sup> Propellant Flow Rate, $\dot{m}_p$ , A (Equivalent)	Ratio of Doubly-Charged Ion Current to Total Current, %	Thrust Reduction Factor, $\alpha$	Thrust Reduction Factor, $F_t$	Propellant Utilization Factor, $\beta$	Total Efficiency Factor $\eta_F^c$
0.5	1100	500	37	2.5	3.5	185	689	49.7	79.8	67.9	0.6	0.136	0.776	2.5	0.991	0.990	0.987	0.986
↓	↓	↓	↓	2.7	1.1	200	696	50.9	79.0	70.6	0.601	0.107	0.748	2.6	0.992	↓	0.987	0.964
↓	↓	↓	↓	3.0	5.0	220	707	48.9	77.8	68.8	0.601	0.126	0.767	2.8	0.992	↓	0.986	0.964
↓	↓	↓	↓	3.4	3.7	250	722	46.6	76.2	66.9	0.59	0.157	0.787	3.2	0.991	↓	0.984	0.961
0.65	800	300	33	3.3	2.7	185	685	48.6	75.9	70.0	0.80	0.128	0.968	4.4	0.987	↓	0.978	0.955
↓	1100	500	↓	5.0	5.5	↓	1138	62.1	82.2	83.0	1.095	0.110	1.245	7.0	0.979	0.992	0.965	0.941
↓	↓	↓	↓	↓	5.7	↓	↓	62.5	↓	83.5	1.08	0.117	1.237	7.4	0.978	↓	0.963	0.941
↓	↓	↓	↓	↓	4.0	↓	↓	62.4	↓	83.1	1.07	0.151	1.241	7.3	0.978	↓	0.963	0.941
↓	↓	↓	35	5.7	3.1	200	1353	58.1	81.3	77.5	1.17	0.120	1.11	5.8	0.983	↓	0.971	0.951
↓	↓	↓	37	5.4	3.8	↓	↓	61.7	↓	81.0	1.09	0.115	1.245	7.0	0.980	↓	0.965	0.945
↓	↓	↓	39	5.1	4.1	↓	↓	62.6	↓	85.1	1.06	0.112	1.212	8.0	0.974	↓	0.956	0.934
↓	↓	↓	↓	4.75	1.9	185	1338	61.9	82.2	82.9	1.09	0.117	1.247	7.8	0.977	↓	0.961	0.939
↓	↓	↓	↓	6.8	3.2	250	1405	59.3	78.3	83.7	1.08	0.115	1.235	8.5	0.975	↓	0.957	0.935
1.15	800	300	37	5.75	4.0	185	1186	56.3	77.4	79.0	1.335	0.120	1.495	6.3	0.982	0.990	0.969	0.945
↓	1100	500	↓	7.5	1.55	↓	1987	67.0	83.0	90.4	1.55	0.109	1.699	11.1	0.967	0.991	0.944	0.922
↓	↓	↓	↓	↓	4.0	↓	↓	67.0	↓	89.9	1.55	0.120	1.710	11.7	0.966	↓	0.941	0.920
↓	↓	↓	↓	↓	5	↓	↓	66.8	↓	89.0	1.55	0.136	1.725	10.7	0.959	↓	0.945	0.926
↓	↓	↓	39	7.1	1.9	↓	↓	68.4	↓	91.4	1.535	0.107	1.682	11.1	0.968	↓	0.945	0.924
↓	↓	↓	41	6.8	4.1	↓	↓	68.6	↓	92.9	1.50	0.115	1.655	13.0	0.962	↓	0.945	0.915
↓	↓	↓	37	8.1	3.2	200	2009	67.1	82.1	91.0	1.55	0.099	1.609	11.5	0.966	↓	0.941	0.920
2.0	↓	↓	↓	10.0	2.8	185	2635	70.9	83.5	95.5	2.00	0.094	2.134	14.8	0.957	0.994	0.926	0.905
↓	↓	↓	↓	↓	5.55	↓	↓	70.2	↓	94.5	2.01	0.107	2.157	14.5	0.958	↓	0.929	0.907
↓	↓	↓	↓	↓	3.7	↓	↓	70.6	↓	94.8	2.0	0.110	2.15	14.1	0.959	↓	0.940	0.909
↓	↓	↓	↓	↓	5.0	↓	↓	69.5	↓	93.4	2.01	0.133	2.18	14.3	0.958	↓	0.928	0.907
↓	↓	↓	19	1.5	3.9	↓	↓	70.3	↓	94.8	2.0	0.110	2.15	14.7	0.957	↓	0.926	0.905
↓	↓	↓	↓	11.4	2.0	200	2665	69.2	82.6	93.0	2.06	0.091	2.19	12.6	0.963	↓	0.917	0.916
2.5	↓	↓	↓	10.8	1.4	↓	↓	69.8	↓	94.9	1.99	0.118	2.148	14.4	0.958	↓	0.928	0.907
↓	↓	↓	37	12.5	2.5	185	3283	70.6	83.8	94.7	2.56	0.080	2.68	15.1	0.956	↓	0.925	0.903
↓	1100	600	↓	↓	↓	↓	3781	73.7	85.9	97.7	2.48	0.080	2.60	16.6	0.951	↓	0.917	0.894
2.75	1150	↓	↓	13.75	↓	↓	3748	72.2	84.4	97.5	2.72	0.100	2.86	16.9	0.950	↓	0.915	0.892

<sup>a</sup>Magnetic baffle control coil has 10.5 turns.

<sup>b</sup>Assumes following neutralizer parameters:  $V_{NK} = 15$  V,  $I_{NK} = 1.5$  A,  $V_b = 12$  V, mercury flow rate = 0.040 A (equivalent).

<sup>c</sup>Discharge chamber only.

ORIGINAL PAGE IS  
OF POOR QUALITY



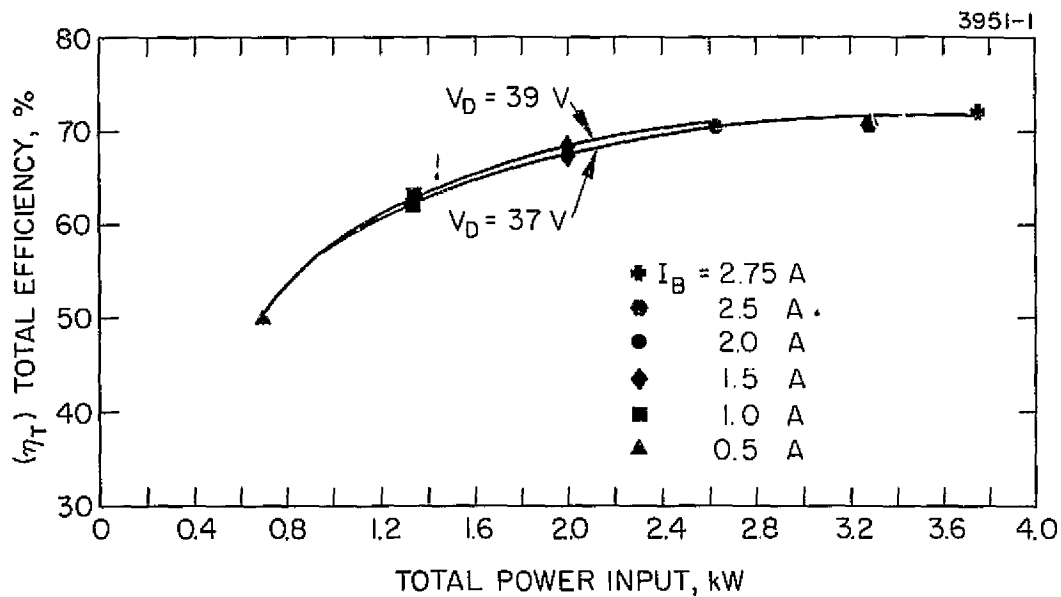


Figure 3. Power/efficiency throttling characteristic for operation at constant discharge loss (185 eV/ion) for 37 V and 39 V discharge voltage.

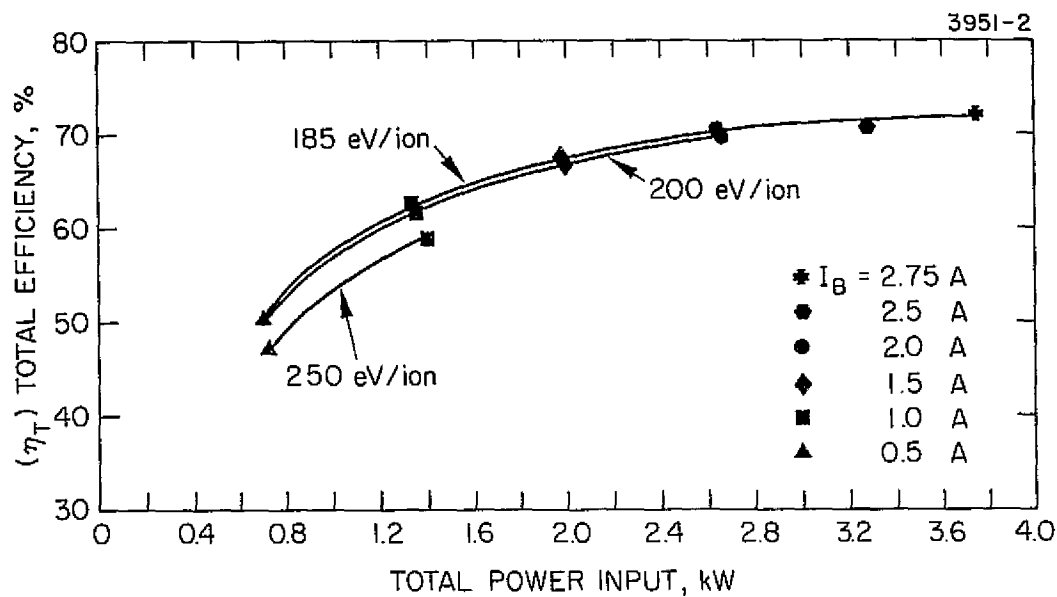


Figure 4. Power/efficiency throttling characteristics for operation at constant discharge voltage (37 V) and constant discharge losses of 185, 200, and 250.

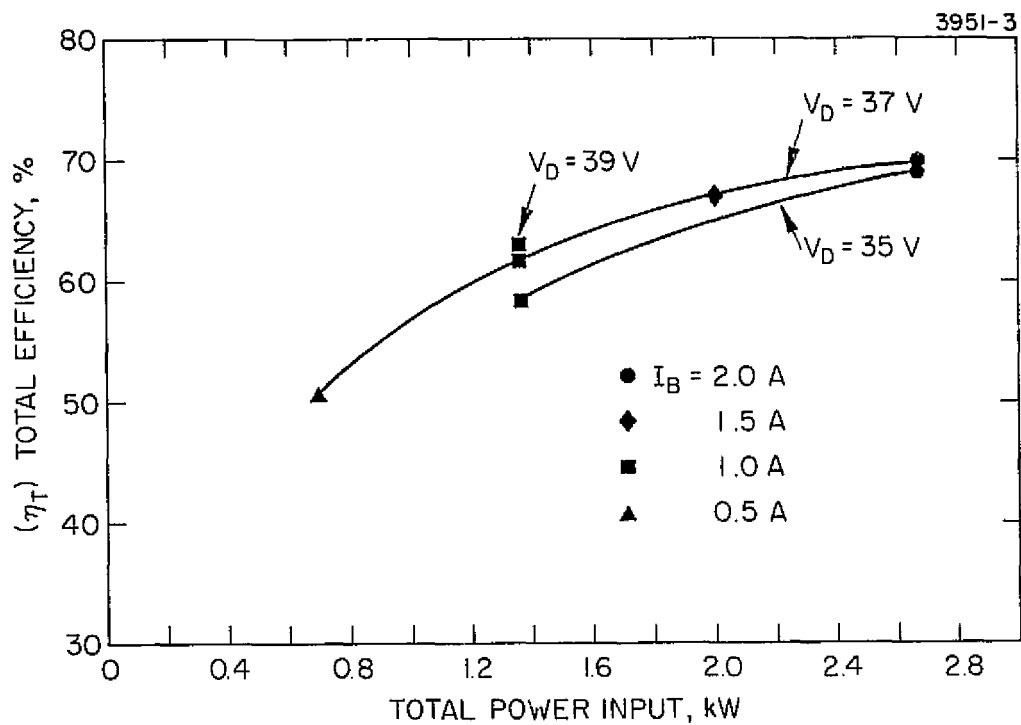


Figure 5. Power/efficiency characteristic for operation at constant discharge loss (200 eV/ion) and discharge voltages of 35 V, 37 V, and 39 V.

operation offered by the use of a magnetically controlled baffle which provides relatively independent control of discharge voltage, current, and cathode propellant flow rate. Since the 30 cm thruster was optimized at the 2 A beam current level, an optimum data point\* has been selected from Table I to compute the loss rate of un-ionized propellant,  $\dot{m}_1$ , by the relation

$$\dot{m}_1 = \dot{m}_0 - I_B \beta = 0.274 \text{ A (equivalent)} . \quad (4)$$

The theoretical curve is then generated by using the values of  $\eta_p$ ,  $\alpha$ ,  $\beta$ ,  $F_t$ , and  $P$  from Table I for each beam current,  $I_B$ , and calculating the total corrected efficiency by the equation

$$\eta_T(P) = \frac{I_B}{(\beta I_B + 0.274)} \eta_p \alpha^2 F_t^2 . \quad (5)$$

Figure 6 shows the remarkably good agreement obtained when the curve generated using eq. (5) is compared with measured values for Table I. Thus, the phenomenological validity of Kaufman's propellant utilization theorem is supported by the results obtained here. If one accepts this theorem, then the throttling characteristic generated by eq. (5) represents the maximum achievable characteristic and the variations shown in Figs. 3, 4, and 5, are expected to have equal or lower  $\eta_T$  values, at best.

## 2. Magnetic Baffle Effects

It can also be seen in Table I, that for any given discharge voltage and discharge loss value, the cathode propellant flow rate is directly proportional to magnetic baffle current. Choice of magnetic baffle current is based on stabilizing discharge operation to prevent mode shift<sup>7</sup> (whereby the discharge voltage is no longer controllable in the "normal" range by cathode flow rate). Optimum propellant

\* First entry in Table I at 2 A beam current and using 32 mA equivalent neutralizer flow (best point from neutralizer mapping).

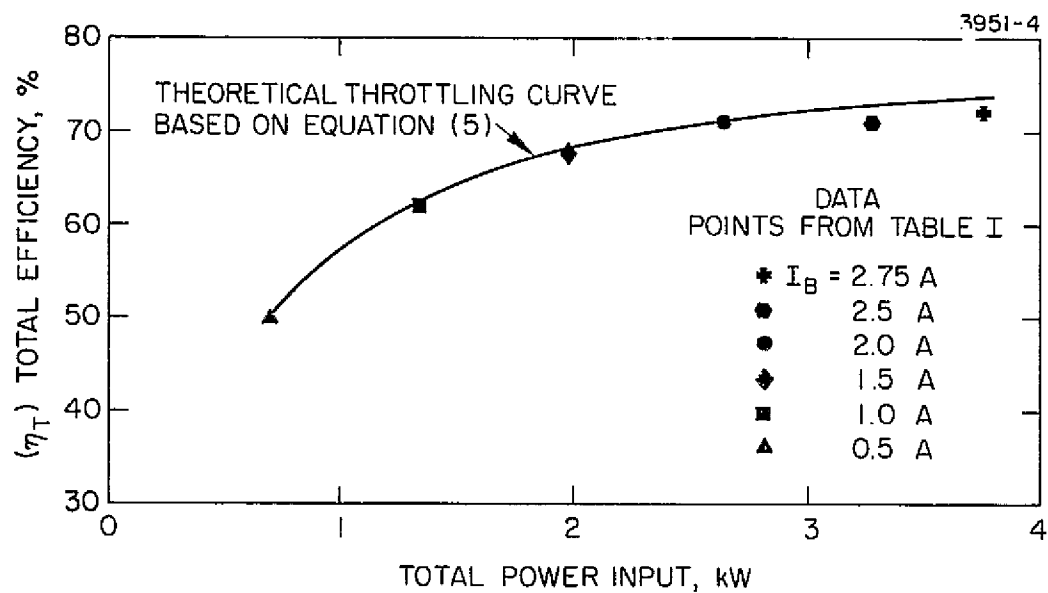


Figure 6. Comparison of power/efficiency characteristics calculated using Kaufman's maximum propellant efficiency theory (accounting for double ionization) with thruster data from this investigation.

efficiency is consequently obtained at the minimum cathode propellant flow rate which is greater than the instability limit and control of the magnetic baffle to satisfy this condition ranges from 30 to 40 ampere-turns for a 5.4 cm diameter baffle.

### 3. High Power Operation

As noted in Table I there are three data points which were obtained at beam current levels above the nominal 2.0 A. These points were considered precursors to the 4.0 A beam operation, and served to identify any obvious thruster problems which may need attention. Thus, a little more discussion is in order concerning operation at these power levels.

At both the 2.5 A and 2.75 A beam current levels the thruster operated satisfactorily with no apparent problems such as excessive temperature excursions or shorting of the accelerator grids. Due to power conditioning limitations, operation at 3.0 A beam current was maintained for only a short time, but the thruster itself appeared to operate quite well. At these higher power levels, cathode tip temperatures remained in the 900 to 1000°C range and isolator temperatures were within the 250 to 300°C range. Although the thruster could continue to operate at 185 eV/ion, the total extraction voltage had to be increased to the 1750 to 1900 V range in order to avoid operation near the perveance limit. Judging from the periods of thruster operation at higher power levels there appears to be no significant reason why continued operation at these and higher power levels cannot be maintained. The amplitude of the discharge oscillations continued to decrease at higher beam currents, and as a result both the beam and discharge control functions were very stable.

### 4. Thermal Data

In the process of collecting the performance data shown in Table I, steady-state operating temperatures were recorded at the locations shown in Fig. 7. Table II gives typical values for these temperatures for a number of the operating points given in Table I.

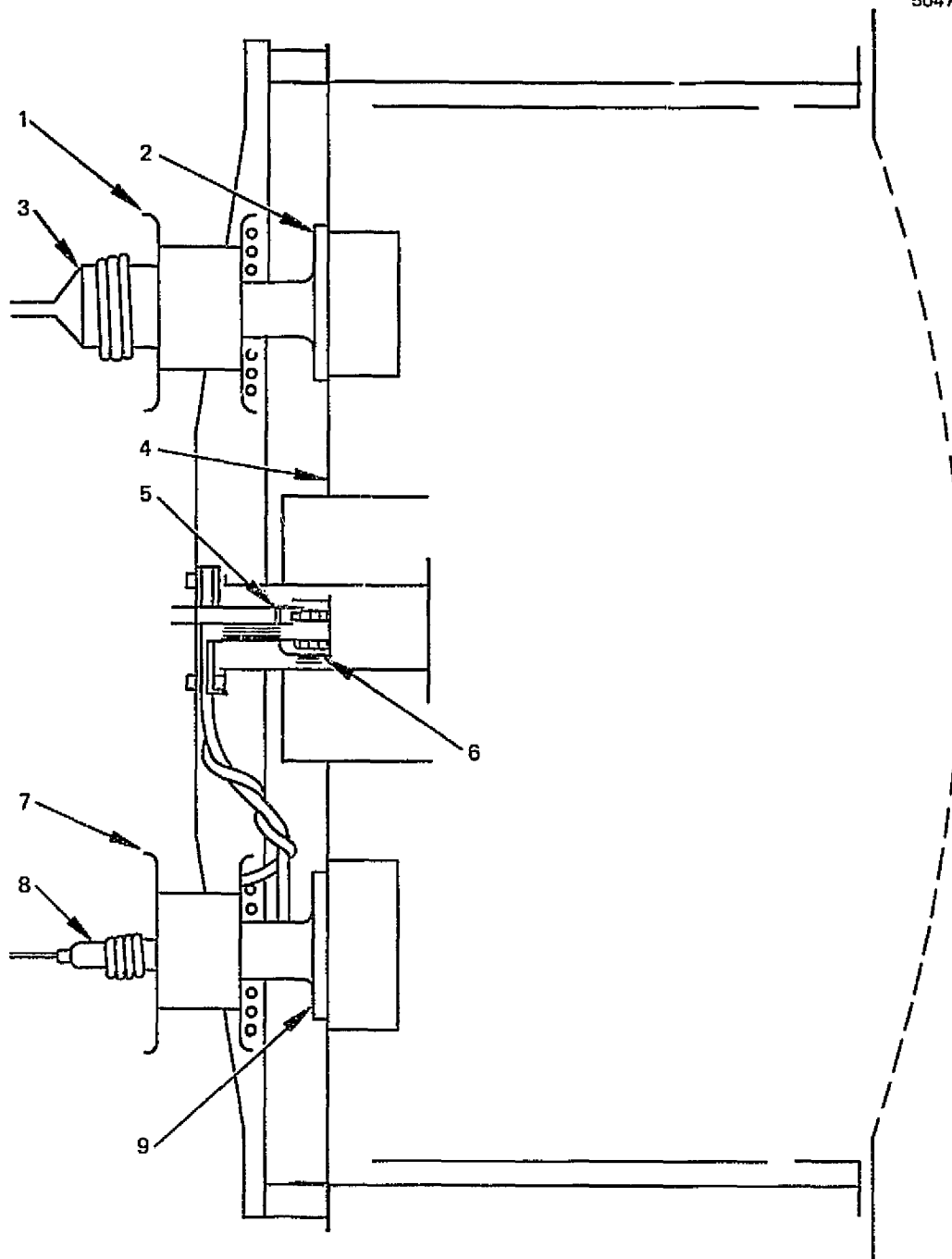


Figure 7. Schematic drawing of thruster discharge chamber showing thermocouple locations for data given in Table II.



Table II. Engineering Model Thruster Thermal Data

Beam Current, A	Discharge Voltage, V	eV/Ion	Isolator Heater Power, W	1 Main Isolator °C	2 Main Isolator Base, °C	3 Main Vaporizer, °C	4 Magnet Retainer, °C	5 Cathode Tube, °C	6 Cathode Tip, °C	7 Cathode Isolator, °C	8 Cathode Vaporizer, °C	9 Cathode Isolator Base, °C
0.5	37	185	7.5	233	213	260	159	485	575	243	315	198
0.5	37	185	5.0	230	209	210	158	485	580	240	315	192
0.5	37	200	6.0	232	209	260	155	470	572	245	310	205
0.5	27	220	6.0	232	212	260	166	500	600	250	216	211
1.0	37	185	7.0	252	235	279	208	578	695	250	304	218
1.0	37	185	0	231	194	280	200	569	695	227	308	181
1.0	39	185	4.0	230	191	280	202	570	680	243	208	211
1.0	37	200	4.0	240	212	280	210	585	710	245	308	214
1.5	37	185	0	246	219	291	233	610	765	235	304	206
1.5	39	185		242	218	292	235	655	775	234	304	205
1.5	37	200		245	220	291	240	637	785	237	299	210
2.0	37	185		258	239	301	262	640	822	242	302	225
2.0	39	185		256	236	299	262	670	832	245	301	223
2.0	37	200		258	240	301	270	680	840	247	305	230
2.5	37	185		268	256	311	290	700	870	256	301	250

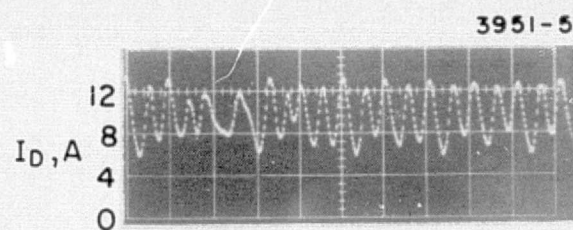
T1606

ORIGINAL PAGE IS  
OF POOR QUALITY

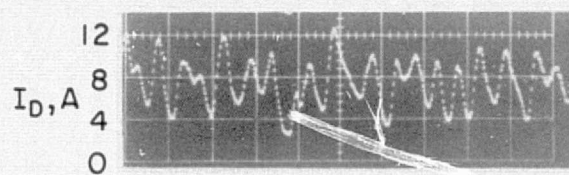
Neutralizer thermal data has again been omitted because the neutralizer used was not suitably representative of the EMT design. The only component temperatures which are not totally satisfactory during typical operation are the isolator temperatures at low power operation ( $<1300$  W). These components require heater power (normally used only during startup) to prevent propellant condensation. Cathode tip and insert temperatures remain in a satisfactory range even up to the 2.5 A beam current level. It is anticipated that all of the component designs would be satisfactory from a thermal standpoint even at higher beam currents.

#### 5. Oscillations

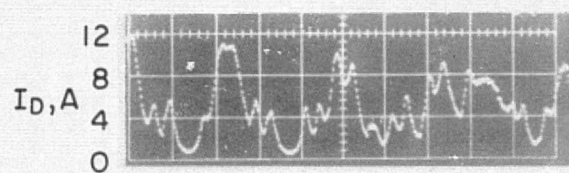
One characteristic of thruster performance which cannot be adequately explained with regard to either cause or effect is the oscillatory behavior observed in the discharge chamber. These oscillations are manifested primarily as a modulation of the discharge current with lesser modulation of discharge voltage and beam voltage and current. The amplitude and frequency of this modulation depends on several factors such as magnetic baffle control current, cathode propellant flow rate, discharge voltage, and configurational parameters which affect the magnetic field in the cathode orifice region. Oscillation amplitude and frequency can also be influenced by power processor output characteristics.<sup>8</sup> Typical waveforms of discharge current for 3.5 A magnetic baffle current at four beam current levels are shown in Fig. 8. It can be seen that the peak-to-peak modulation amplitude remains approximately the same at each beam (discharge) current, thereby increasing the percentage of modulation with decreasing beam (discharge) current. The fundamental frequency at full beam power operation is approximately 20 kHz and the oscillation is quite periodic and stable. Lower frequencies appear and tend to dominate at lower discharge currents. The current is very nearly interrupted at a 2.5 kHz rate at the 0.5 A beam point. Synchronized waveforms of discharge current and voltage indicate that these quantities are out of phase by approximately 90 to 180 degrees. Very little more can be said about these oscillations, although operating conditions have been found which essentially eliminate them.<sup>8</sup> No evidence has been



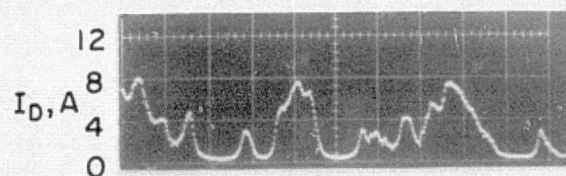
(a)  $I_B = 2.0 \text{ A}, I_D = 10 \text{ A}$



(b)  $I_B = 1.5 \text{ A}, I_D = 7.5 \text{ A}$



(c)  $I_B = 1.0 \text{ A}, I_D = 5.0 \text{ A}$



(d)  $I_B = 0.5 \text{ A}, I_D = 2.5 \text{ A}$

Figure 8. Comparison of discharge current waveforms for four beam current values as noted. Time scale is  $100 \mu\text{sec/div.}$

established to substantiate any loss of efficiency, or increased doubly-charged ion production which can be associated with these oscillations. These oscillations are somewhat troublesome to power processor and control functions, however, especially at the lower beam current operating points. Except at lower beam operation where discharge current is nearly interrupted, the beam current fluctuations are observed to be negligibly small and uncorrelated with discharge current oscillations. This indicates that the observed oscillation is more a variation in electron transport process than in plasma density or ionization process. The only conclusion that can be reached at this time based on this observed oscillatory behavior is that extension of thruster operation to higher power levels, rather than lower power levels, would be preferable.

#### 6. Erosion Monitors

Erosion of thruster components was monitored throughout the performance mapping tests by several techniques and in a number of locations. Since backspattered deposition from the steel beam target is a competing process, only areas where sputter erosion is relatively severe were observed to display material loss, most of the locations showing either no loss or a coating. Careful analysis of these coated surfaces would be required to deduce erosion rates and this was not attempted. Consequently, only two thruster components could be quantitatively analyzed for erosion rate. The neutralizer cover plate was monitored using an "erosion badge" on which eight layers of copper and chromium were deposited in alternating layers of 1000 Å and 250 Å, respectively. (This provides approximately equal sputtering times per layer.) Erosion was observed from the downstream-most tip of the neutralizer cover to the point at which the thruster cover shields the neutralizer from the ion beam. Erosion rate was equivalent to 50 Å/hour for chromium. The other location which showed measurable erosion was the downstream surface of the baffle. Initial attempts to monitor erosion of this surface using the alternating layer technique were unsuccessful because the layers were completely

removed in the test times allotted between inspections. A successful semiquantitative measurement was completed by fastening a thin, highly polished and coated silicon wafer to the baffle surface. The coating on the wafer was a sputter-deposited layer of steel, 6000 Å thick. The wafer was masked in several areas to provide "bench marks" for obtaining a depth measurement with a precision profilometer. After 20 hours of operation, the step measured from the bench mark region was approximately 7000 Å, or 350 Å eroded per hour. Several repetitions of this experiment at different baffle locations yielded erosion rates from 200 to 500 Å per hour with erosion rates being highest near the baffle center and edge. These measurements are considered to be minimum erosion rates since erosion and deposition are competing processes and the silicon wafer is suspected of charging somewhat because of its lower conductivity. On the basis of these rates, the baffle should not be eroded away until approximately 20,000 hours of operation, which is about a factor of three greater than observed in the endurance test described by C. Collett.<sup>9</sup> Consequently, it must be concluded that for measurement of sputtering erosion using the techniques described above, greater care must be taken to prevent charging of the sample being studied, and that backspattered beam target deposition must either be eliminated (through use of a frozen mercury collector) or accounted for in some indirect manner.

#### C. Additional Results

##### 1. Neutralizer Studies

Prompted by abnormalities that were observed during the performance mapping, and in the endurance test of thruster S/N 701, further investigation of an 800 series neutralizer was conducted. The purpose of this phase of testing was to characterize a new neutralizer (S/N 806) and to observe its characteristics with time so that a basis for future remedial action could be established. Control curves for

the new neutralizer are shown in Fig. 9(a) for various beam current levels, where keeper voltage is plotted as a function of vaporizer temperature. Figure 9(b) shows the variation in floating potential for these same points. Throughout all tests the neutralizer keeper current was maintained at 1.5 A. After approximately 6 hours of operation the 2.0 A beam condition was repeated. After it was found that the neutralizer characteristic had shifted to a somewhat higher keeper voltage level, operation was then continued at full power to observe any further changes in performance. The curves of Fig. 10(a) show the various keeper voltage functions after accumulating the time as indicated, while Fig. 10(b) again shows the floating potential variations. In general, there seems to be a decrease in the slope of the control curve with time, and after approximately 32 hours of operation a more dramatic shift in voltage was noted. This particular higher voltage characteristic was first obtained when high frequency power conditioning was substituted for the 60 Hz supplies. However, a return to the low frequency supplies did not restore the preceding control characteristic and the neutralizer continued to operate on this higher voltage control characteristic.

The variation in control characteristics exhibited by this neutralizer was very similar to the characteristics observed with the life test neutralizer S/N 701 where two modes of operation were noted. In the life test the shifting appeared to be random and operation in any one of the modes would continue for many hours. The less dramatic shifting of the keeper voltage versus propellant flow characteristic has been noted in all 700 and 800 series neutralizers; in particular, the shake test neutralizer (S/N 703) displayed control characteristics similar to those of S/N 806 except that no mode requiring a higher keeper voltage set point ( $\sim 16V$ ) was observed.

Attempting to identify the source of the observed control variations one notes that there appears to be a rather steep thermal gradient along the cathode tube between cathode tip and insert location. Figure 11 shows a schematic drawing of the neutralizer and designates

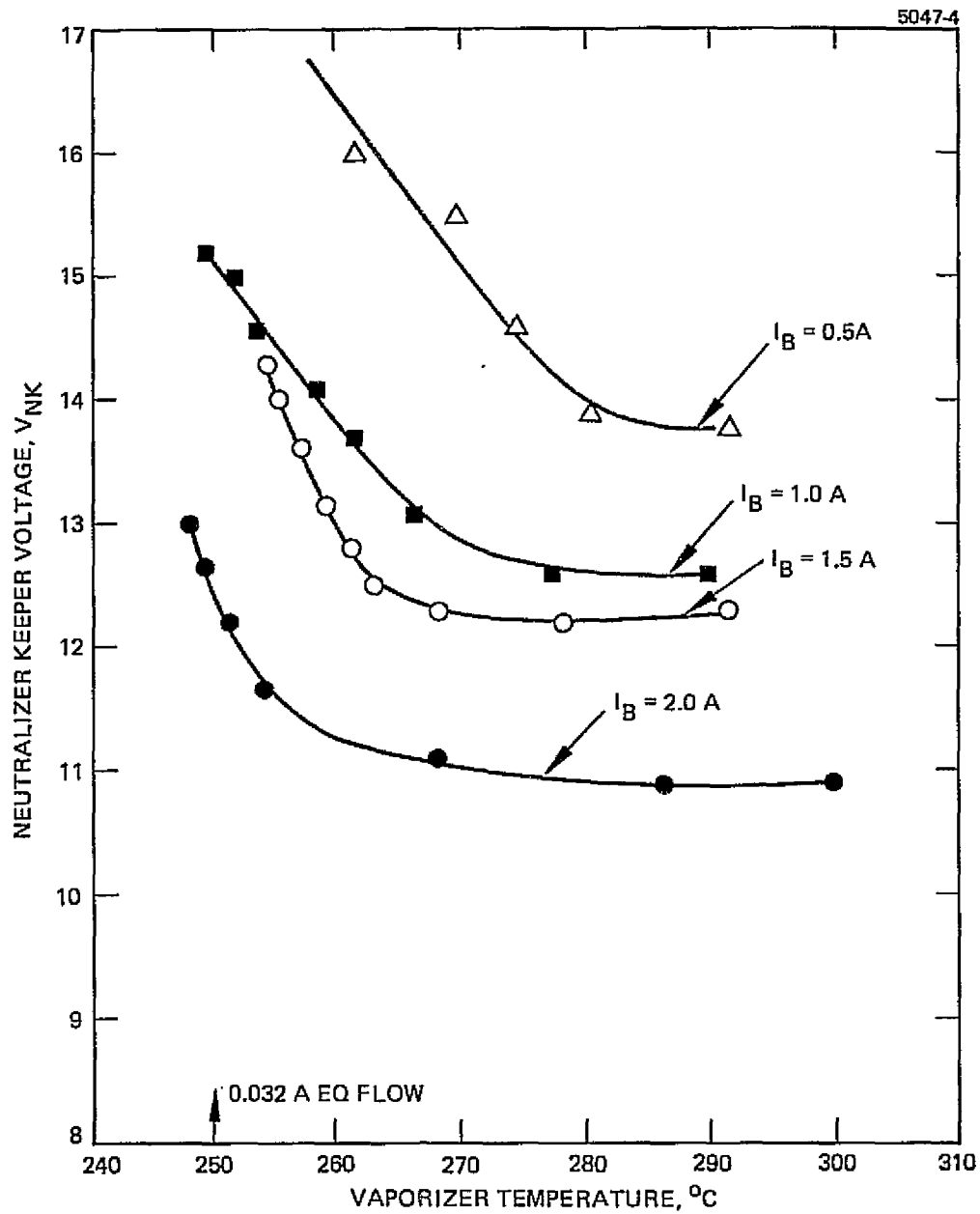


Figure 9(a). Control characteristics for neutralizer 806;  
 $I_{NK} = 1.5\text{ A}$ .

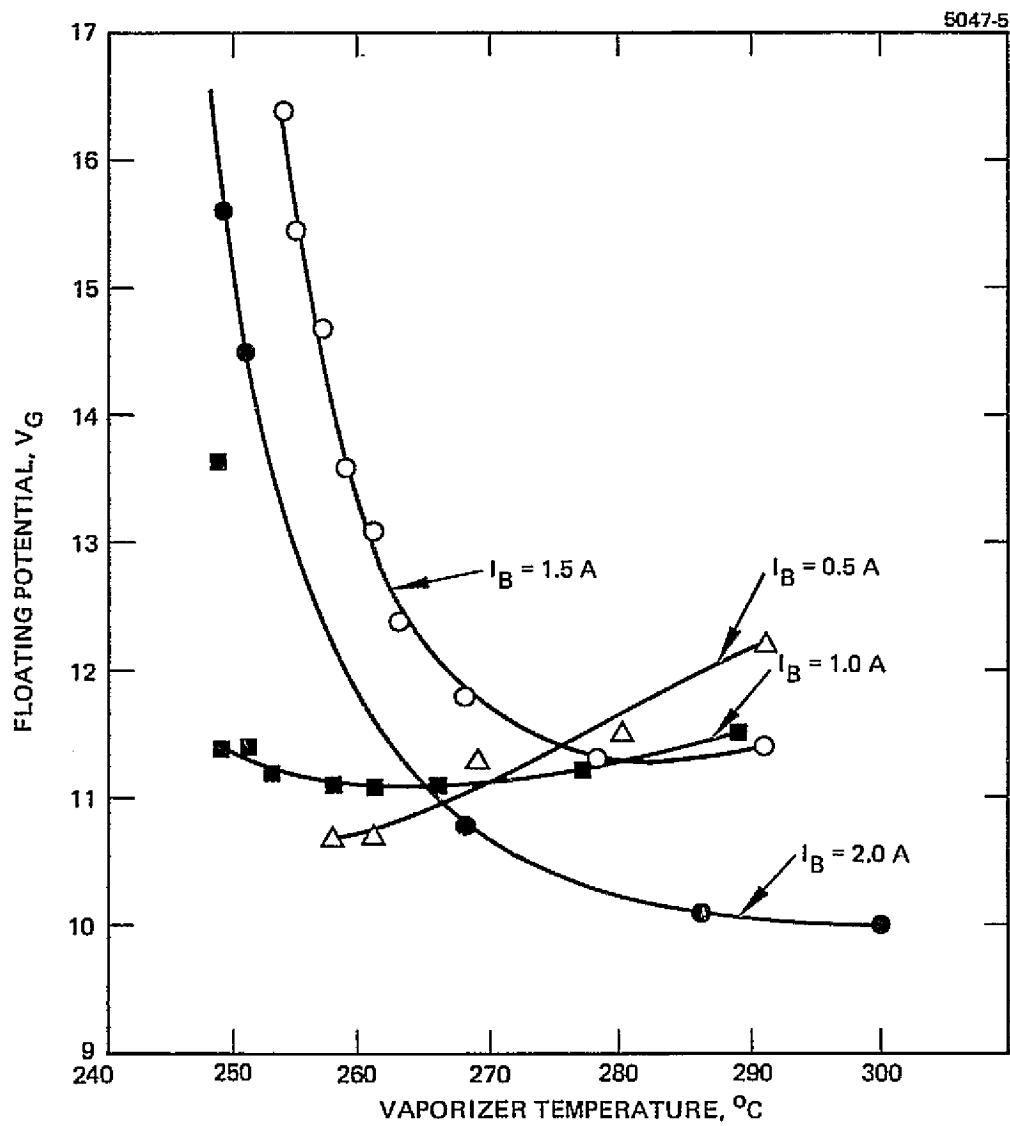


Figure 9(b). Floating potential variations for neutralizer 806;  
 $I_{NK} = 1.5$  A.



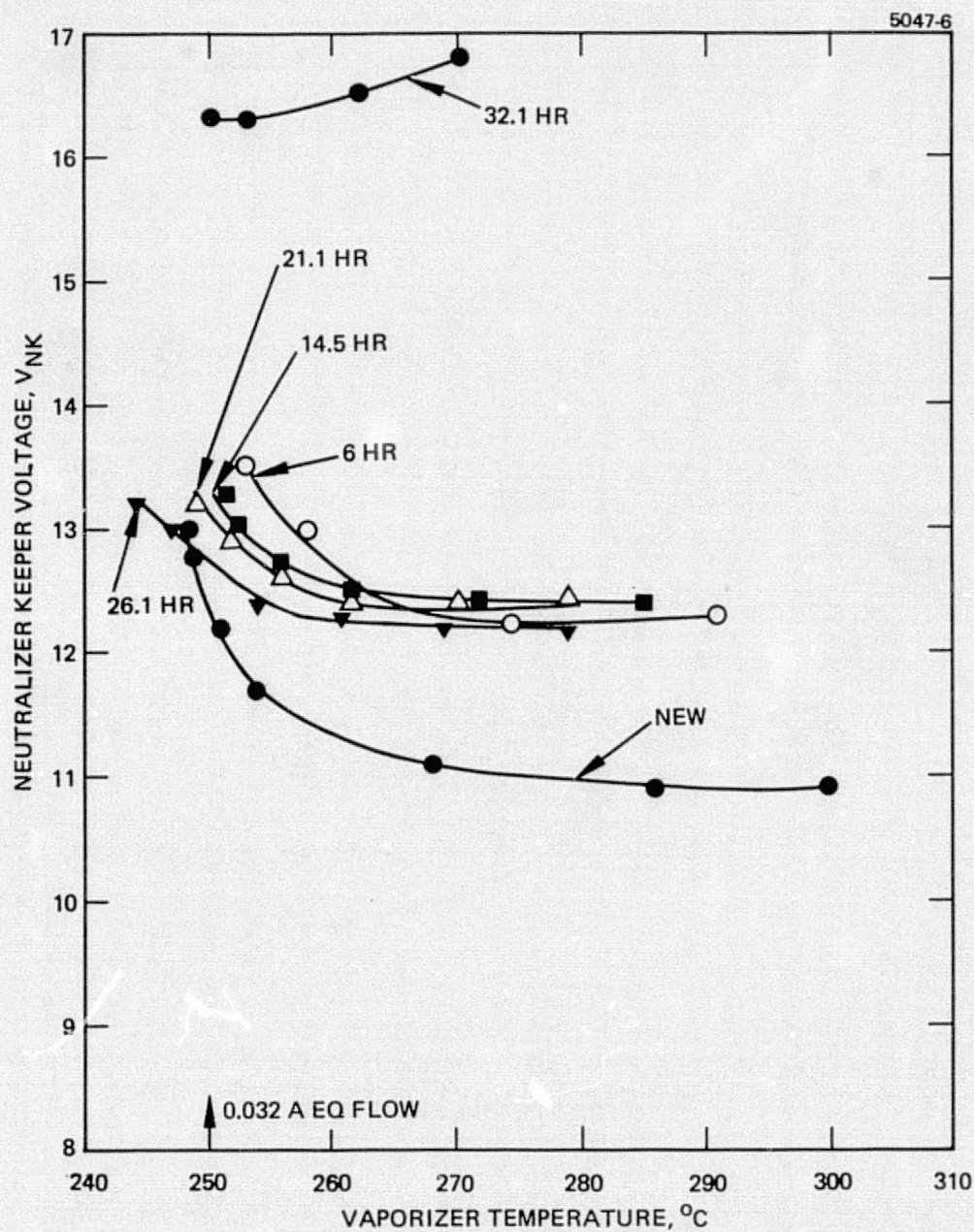


Figure 10(a). Variation in characteristic after accumulated time as indicated.  $I_{NK} = 1.5$  A,  $I_B = 2.0$  A.

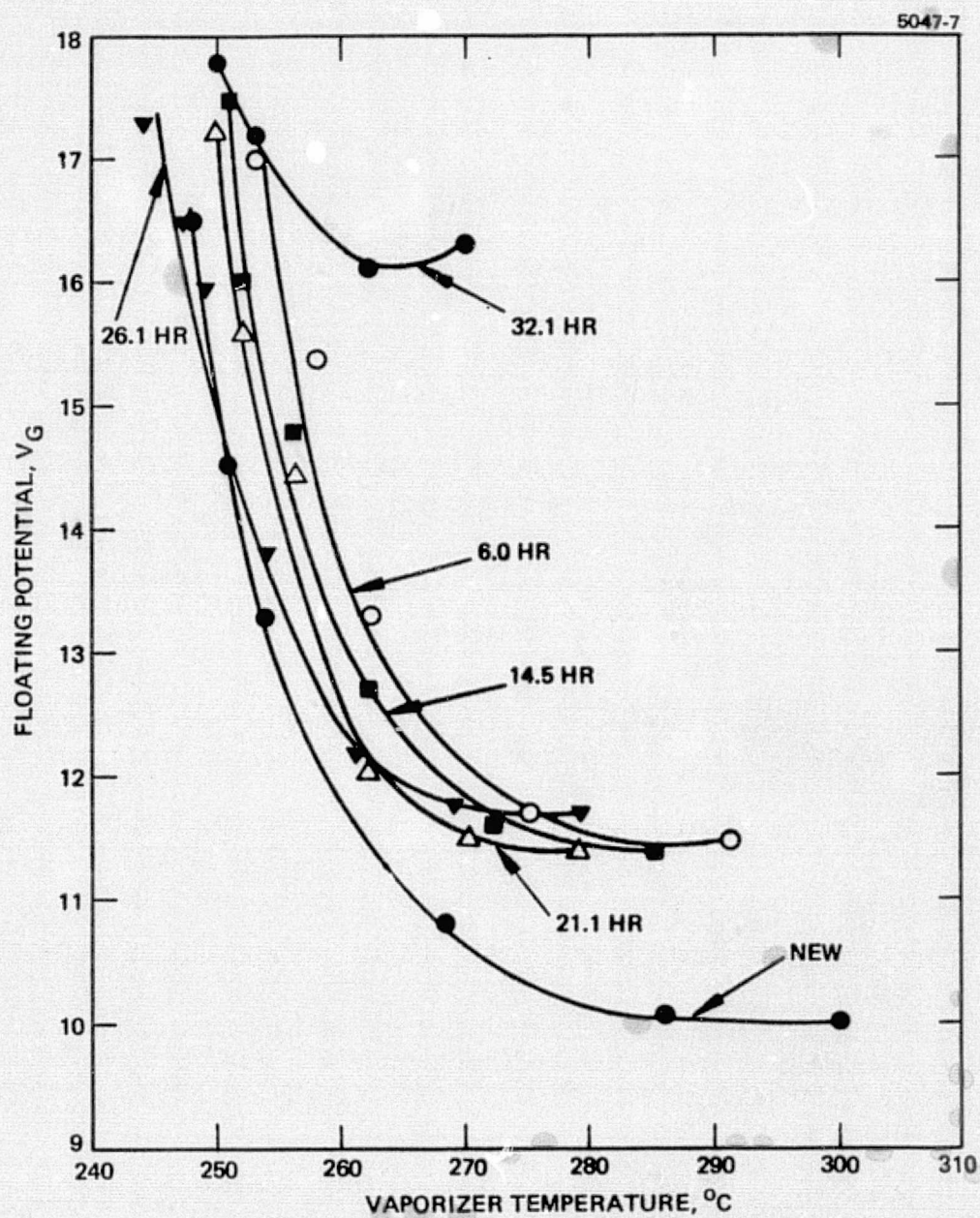


Figure 10(b). Variation of floating potential with time.  
 $I_{NK} = 1.5 \text{ A}$ ,  $I_B = 2.0 \text{ A}$ .

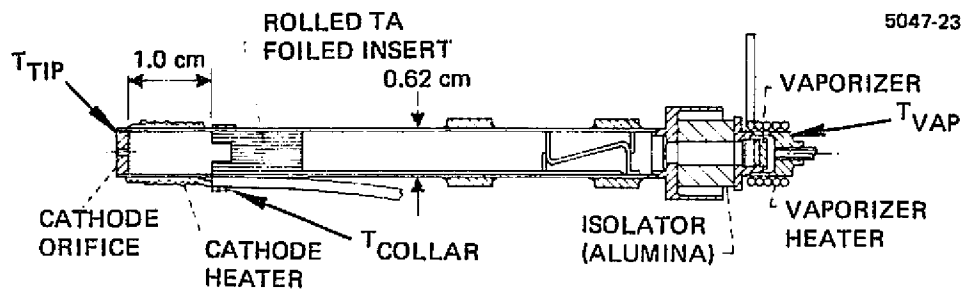


Figure 11. Cross section of neutralizer cathode indicating location of thermocouples.



the thermocouple locations. The temperatures recorded at these locations during the performance mapping of the neutralizer are given in Table III. It appears likely that insert temperature is too low in the desired operating regime to contribute to either emission processes or aid in supplying barium to the higher temperature surfaces downstream of the insert. These results prompted a more in depth investigation at NASA LeRC that resulted in specification of a barium aluminate impregnated porous tungsten insert to replace the coated foil insert.

## 2. Beam Studies

The evaluation of the effluent ion beam from a 30 cm thruster was prompted by a decrease in mass utilization efficiency which was noted during the course of the performance mapping. Upon returning to 2.0 A beam current after considerable operation at 1/2 and 1/4 power levels, it was found that the mass efficiencies had decreased 1 to 2%. An examination of the grid set revealed an increase in the diameter of the accelerator apertures at increasing distance from the thruster centerline. As can be seen from Table IV, the accel aperture size varies in an almost linear fashion with radius. Because of the 0.5% screen grid compensation, the "vectoring" at the edge of the grid is considerable and results in ion crossover in the aperture region. Also, at lower power levels the beam divergence is significantly greater than at full power, as is shown in Fig. 12 where the normalized ion current density is plotted as a function of dispersion angle. Both the 0.5 A beam current and the 2.0 A beam current curves are representative of a radial location of 10.25 cm. Although the absolute current density is less for the 0.5 A condition, operation at these low beam levels for extended periods could result in increased aperture diameter due to direct interception. Based on an average enlarged hole size of 1.68 mm, as compared to the 1.58 mm original size, the equivalent neutral loss difference and subsequent drop in mass utilization could be calculated. Although the calculation was approximate, the indication was that the enlarged accel holes could certainly be responsible for the

Table III. Neutralizer Temperature Variation,  $I_B = 2.0$  A

Operating Time, hr	$T_{NV}, ^\circ\text{C}$	$T_{\eta_p}, ^\circ\text{C}$	$T_{\text{collar}}, ^\circ\text{C}$
New	251	960	555
	254	960	555
	268	975	555
	286	980	560
	300	985	555
6	253	1020	590
	258	1045	595
	262	1050	595
	275	1075	600
	291	1100	605
14.5	251	1010	590
	252	1020	590
	256	1020	590
	262	1030	595
	272	1050	600
	285	1080	610
21.1	249	1000	590
	252	1005	590
	256	1010	590
	262	1030	590
	270	1040	595
	279	1065	600
26.1	244	990	580
	247	990	580
	249	995	580
	254	1010	590
	261	1020	590
	269	1040	600
	279	1060	600
32.1	250	1165	740
	253	1090	740
	262	1130	755
	270	1160	760

T1869

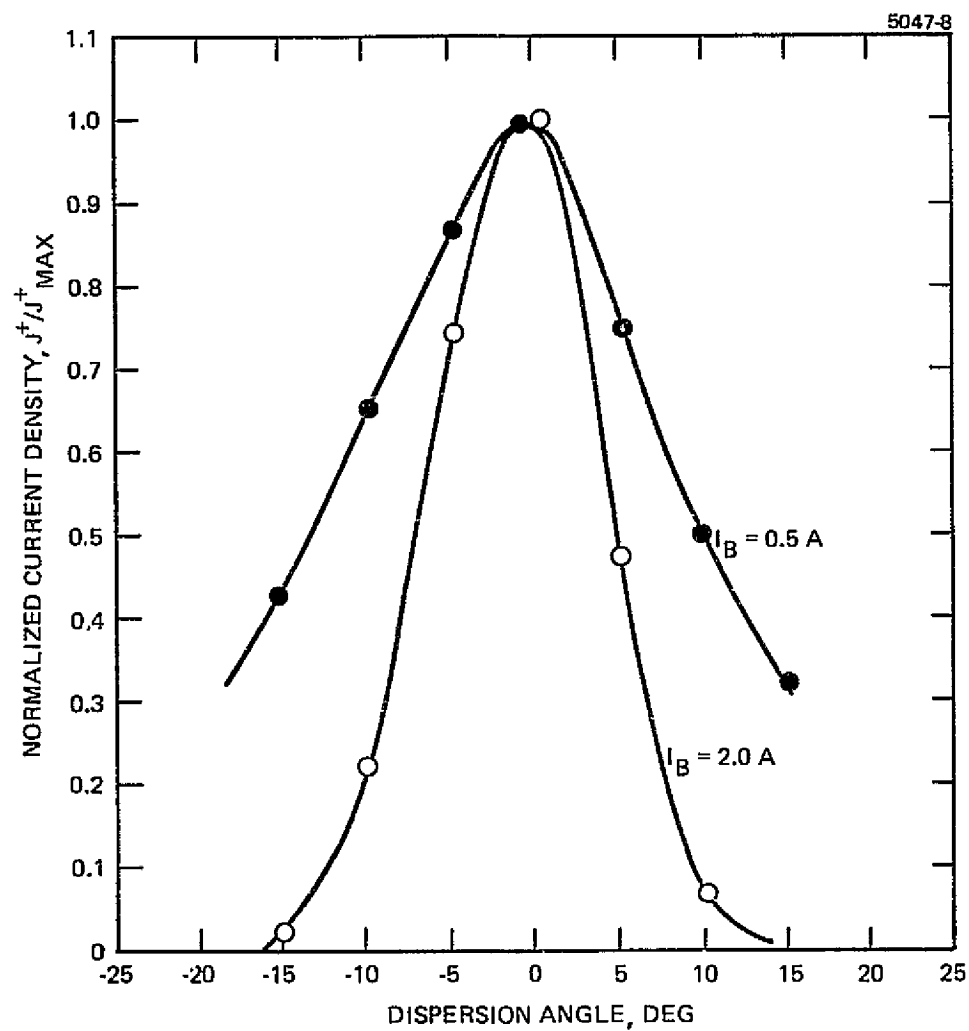


Figure 12. Single ion beam divergence at  $r = 10.9$  cm for beam currents of 2.0 and 0.5 A.

Table IV. Variation of Accel Aperture Diameter  
Across Grid S/N 644

Thruster Radius, cm	-15	-12.5	-10	-7.5	-5	-2.5	0	2.5	5	7.5	10	12.5	15
Accel Aperture Diameter, mm	1.75	1.73	1.70	1.68	1.65	1.61	1.60	1.65	1.68	1.70	1.70	1.70	1.73

T1870

performance drop. Optics S/N 650, which are identical to optics 644 except that they have uniform aperture size, were substituted and the thruster performance was again evaluated. As anticipated, the mass utilization as well as the perveance were restored to the original design conditions. Table V shows the performance parameters for the two optics sets. Based on these results, it appears that the total accelerating voltage must be reduced for lower beam currents to preserve the focusing of the individual beamlets in order to minimize any erosion of the accelerator electrode apertures which result from direct interception.

In conjunction with the beam profiles done for aperture size determination, two more detailed studies of high angle beam trajectories were also done. These studies included primary as well as charge exchange ions. Most of the primary beam ions are well collimated with more than 99% of the beam current contained in a  $20^\circ$  half angle. However, there is a small class of ions, most of which originate near the periphery of the grid which are emitted with angles much larger than the nominal  $15^\circ$  half angle. To measure these fringe ions a narrow angle collimating probe was built to sample the angular current density distribution emanating from a small area on the accelerator grid. Figure 13 shows the geometric configuration of this collimating probe, which allows it to travel in a circular arc while viewing the same grid area. This probe has a  $2^\circ$  acceptance half angle resulting in a 0.7 cm diameter viewing area at a probe-accel distance of 10 cm. Figures 14 and 15 show probe characteristics taken at different accel voltages at the central and edge regions of the accelerator grid. These curves

5047-9

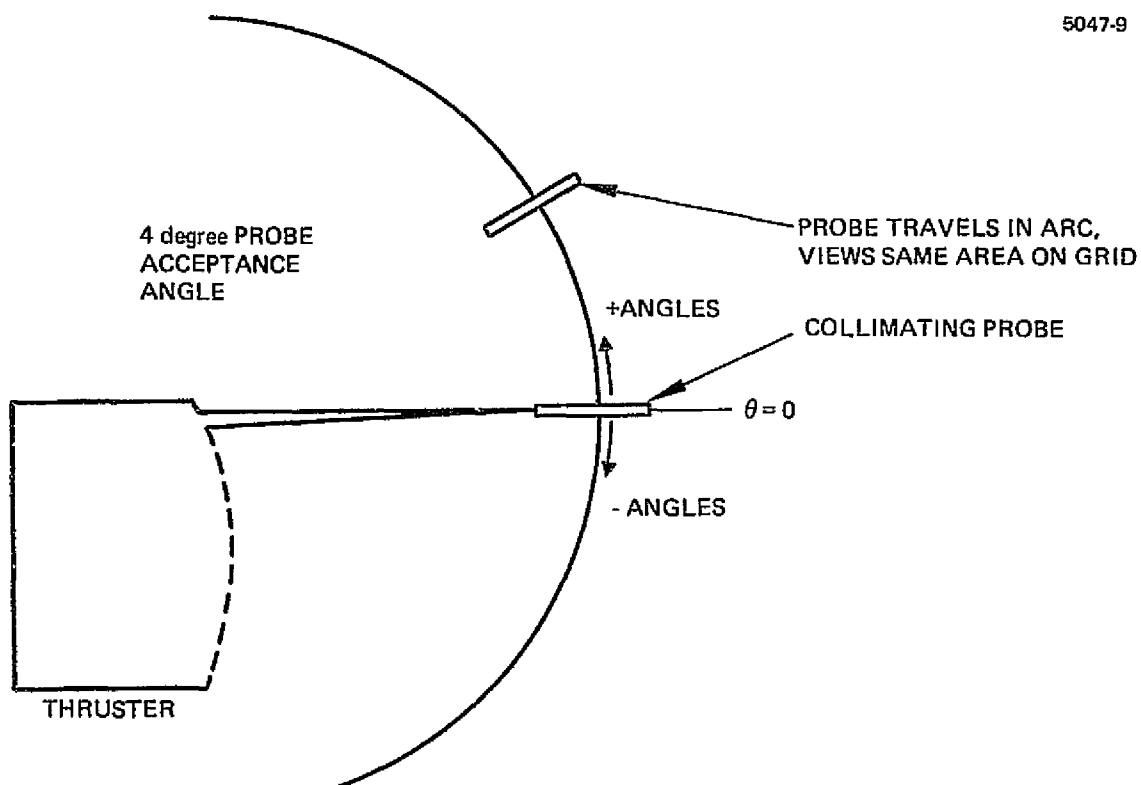


Figure 13. Geometric configuration of collimating probe used to sample angular current density from accel electrode.



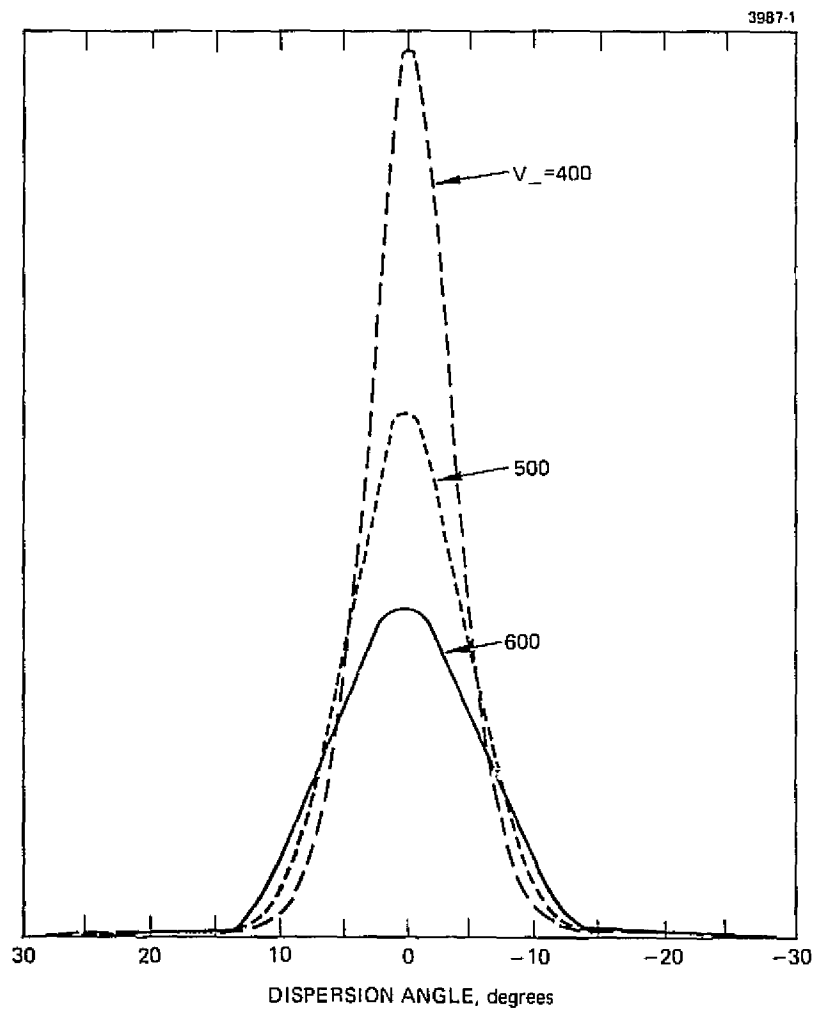


Figure 14. Experimental data showing angular current density distribution emanating from holes on beam center-line for different accel voltages.

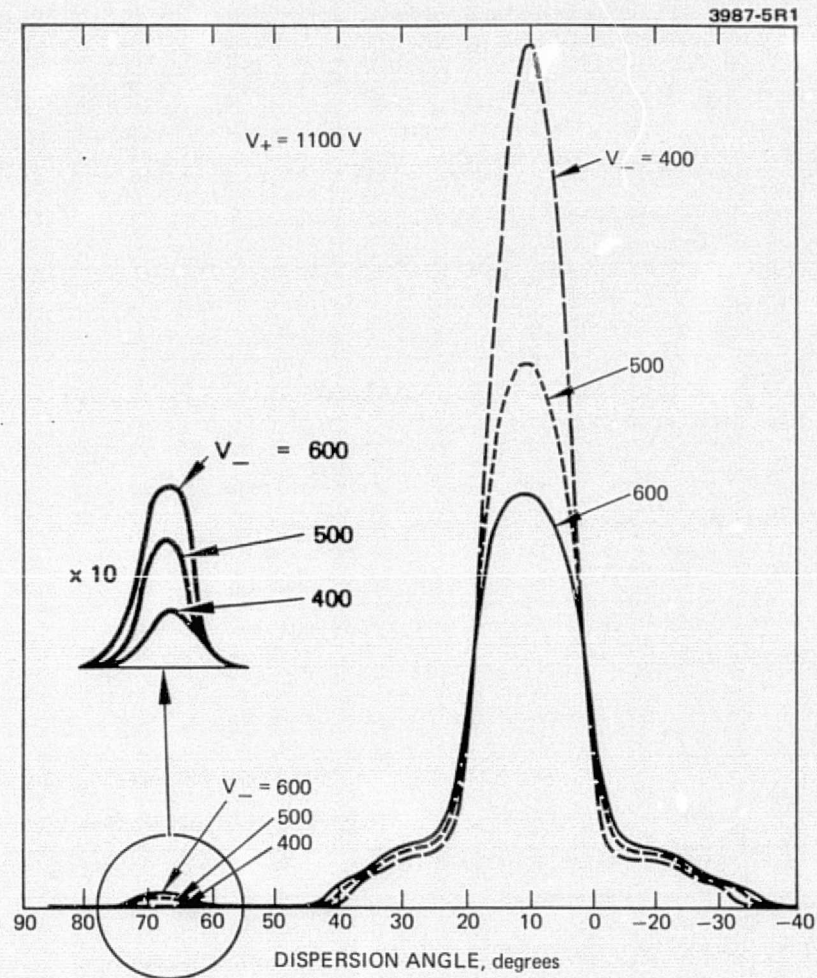


Figure 15. Experimental data showing angular current density distribution emanating from edge holes showing fringe beam ions at high angles.

Table V. Performance Parameters for Optics S/N 650 and S/N 644

Optics	Weighing System			Pipette		
	$\eta_{m \text{ dis' } \%}$	$\dot{m}_{\text{main}}$	$\dot{m}_{\text{cath}}$	$\eta_{m \text{ dis' } \%}$	$\dot{m}_m$	$\dot{m}_{\text{cath}}$
S/N 644	93.4	2.045	0.094	94.2	2.03	0.092
S/N 650	94.3	2.018	0.102	95.2	2.00	0.100

T1871

show how the beamlets from the central region have appreciably less angular divergence than the edge beamlets which originate from a more concave plasma sheath boundary. The traces also show how the profiles become more peaked as the accel ( $V_-$ ) voltage is reduced. The current trace taken at the edge shows a small group of ions which are emitted with angles up to  $80^\circ$ . These ions were not observed until a 1 cm wide slit was cut in the ground screen electrode. The ground screen geometry and placement is at the correct location to intercept these ions. Usually after a few hours of operation the edge of the ground screen facing the edge row of accelerator holes has the characteristic clean appearance of a sputtered surface. Retarding field measurements on these "fringe" ions showed that they had the full beam energy; they were not poorly focused Group 2 charge exchange ions. It was also observed that the height of this current peak decreased with accel ( $V_-$ ) voltage. First attempts at modeling these fringe ions assumed they were crossover trajectories from the corner of the plasma sheath. Computer trajectories showed that it was not possible to simulate the  $80^\circ$  trajectories even with an ion with a 30 eV initial energy directed in the outward radial direction. The fact that the fringe ions were not observed when the accel voltage was reduced to -400 indicated that these ions might be related to the end effect at the beam edge where the virtual ground neutralization plane curves away from the accelerator grid. The field lines between the accel and this virtual ground boundary are in a direction to bend the peripheral ions in an outward direction. As the accel voltage is reduced this force

decreases. Figure 16 shows the beam edge geometry used to model these trajectories. Trajectories were run from the simulated accel electrode making angles of  $20^\circ$  with respect to the edge hole centerline. The assumed neutralization plan was placed a distance of 0.05 in. from the accel electrode. These calculated trajectories do exhibit the behavior observed experimentally. It is seen that the edge trajectories exit with angles from  $60$  to  $80^\circ$  in agreement with the experimental data.

The other experiment performed with the collimator probe was to measure radially directed charge-exchange ions formed in the downstream beam plasma. The probe was mounted perpendicular to the beam centerline and could be moved from a position 4 cm upstream to a position 15 cm downstream of the thruster ground screen. The probe was positioned a distance 6.5 cm outward from the nominal 15 cm beam radius. The experimental measurements in Fig. 17 show that as the probe is moved downstream from the ground screen electrode, the current rises from zero to a peak value at the axial position of the grid centerline. In this region the probe is viewing increasing surface areas of the dished grid which extends outward about 1 cm from the ground screen. Downstream of this peak the current slowly decreases with increasing distance. Comparing the above results with data taken at a probe angle of  $-15^\circ$  (in order to view ions exiting perpendicular to the nominal  $15^\circ$  beam spreading angle) we see that the probe current is down more than an order of magnitude. This indicates that the flux of the Group 4 charge exchange ion is directed predominantly in the radial direction rather than in a direction perpendicular to the beam envelope.

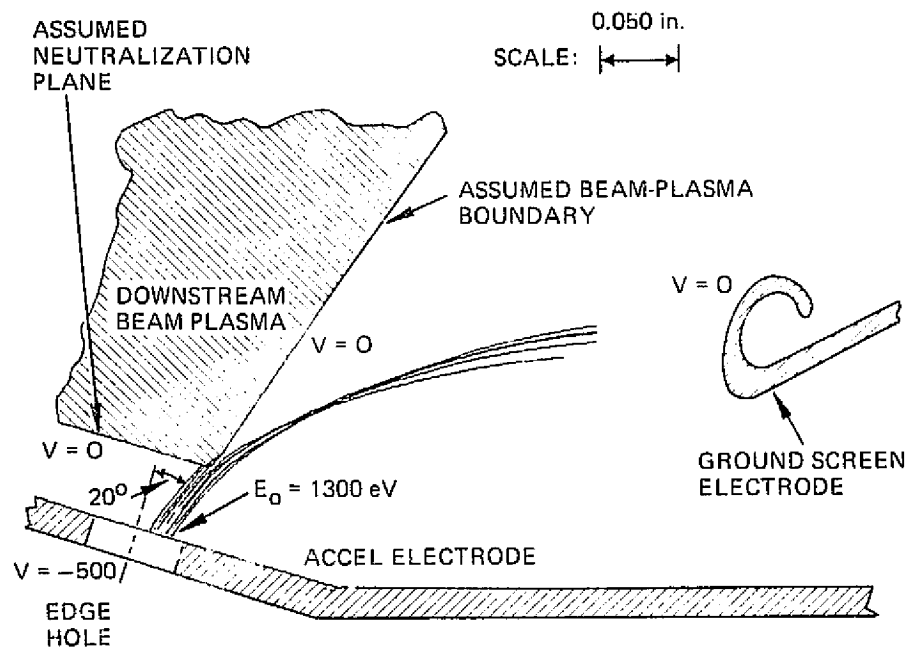


Figure 16. Model used to simulate fringe beam ions which are deflected outward due to the distortion of the virtual ground neutralization plane.

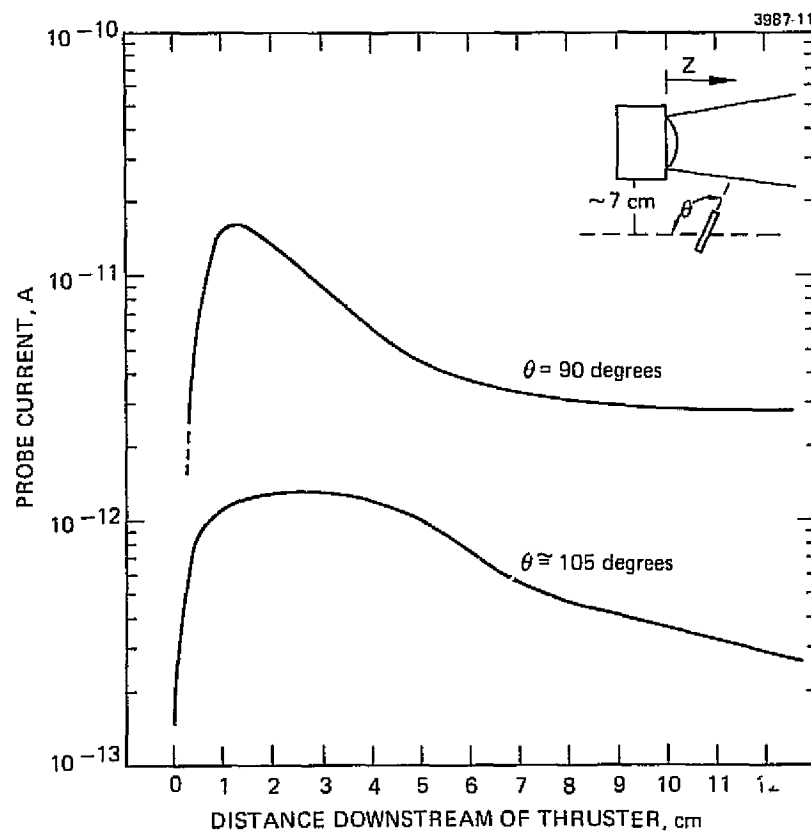


Figure 17. Measured current of radially directed Group 4 charge exchange as a function of distance downstream from ground screen electrode for 0 to 90° and 105°.

### III. DOUBLY-CHARGED ION INVESTIGATION

This section describes the work which was performed to evaluate multiple-ion production and to identify means by which these ion concentrations could be reduced. The detrimental effects of the doubly-charged ion current are manifested in two ways:

1. By an erosion of discharge chamber components, in particular, the baffle and screen grid
2. By a reduced thrust per unit current that results in lower total efficiency.

The first effect is now considered of primary importance although it was the reduction in efficiency that originally motivated this investigation. The intent of this section, therefore, is to describe briefly the apparatus used in this phase of testing and then to summarize and discuss the experimental results that were obtained.

#### A. Beam Probe and Measurement Technique

The ExB mass separator probe was designed and built under previous contracts (NAS 3-16528 and NAS 3-16949). References 8 and 9 describe in detail the entire probing system thus only a brief description of the probing technique and method of data analysis will be given here. Because of the  $0.6^\circ$  probe acceptance angle, the viewing area of the probe at the accelerator grid is approximately  $0.132 \text{ cm}^2$ . Pre-programmed stepper motors position the probe to view selected radial locations in the thruster diameter from various dispersion angles ranging from  $+40^\circ$  to  $-40^\circ$ . Collector currents for both the singly- and doubly-charged ions are obtained from seven dispersion angles at each of four radial locations with the results stored on paper tape. These results provide input data for the computer where the double to single ion current is calculated by averaging overall dispersion angles and radial locations. In addition, the program provides the following information.

1. Thrust and mass efficiency correction factors  $\alpha$ ,  $\beta$ , to account for the presence of doubly-charged ions.
2. Thrust correction factor to account for beam, divergence  $F_t$ .
3. Plots of the radial profiles of the calculated current densities.

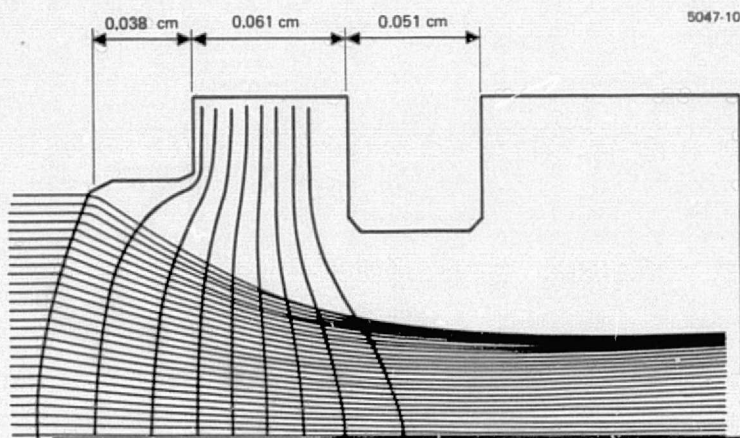
These factors — the data acquisition system, the number of data points used, and the associated averaging effects — make this technique repeatable to within 2%.

#### B. Small Hole Accelerator Grid

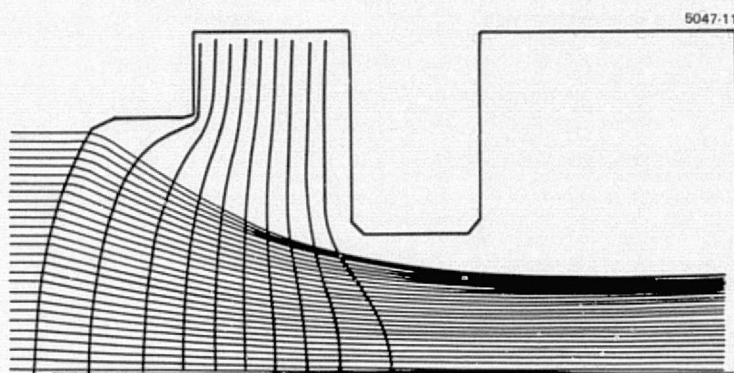
At the outset of the program it was felt that small hole accelerator grid (SHAG) optics would be beneficial in achieving thruster operation at reduced double ion concentrations. Because of the long lead time necessary for grid manufacture, a set of SHAG specifications was a priority item before any testing was to begin. A minimum accel aperture diameter was desirable from the performance viewpoint; however, the holes should not be so small that considerable time would be spent in machining apertures with the added possibility of destroying beam divergence properties by incorrect compensation.

In an effort to establish a minimum accelerator grid open area fraction, two techniques were employed. One technique was to cover apertures in an existing grid set with thin Ta foil, and permitting the beamlet to machine a new aperture. Thruster operation at 2.0 A beam current quickly sputtered the foil and an aperture diameter of 0.089 cm was determined as minimum on the thruster axis. A second technique was to compute the ion trajectories for various accel aperture diameters. Results of the computer analysis are shown in Fig. 18, whereby a reduction of diameter from the present 0.156 cm to 0.103 cm would not result in any direct interception and agrees well with the experimental data. If such a grid were manufactured the open area fraction would be approximately 20%. Table VI summarizes the parameters which were chosen for the manufacture of the SHAG optical system.

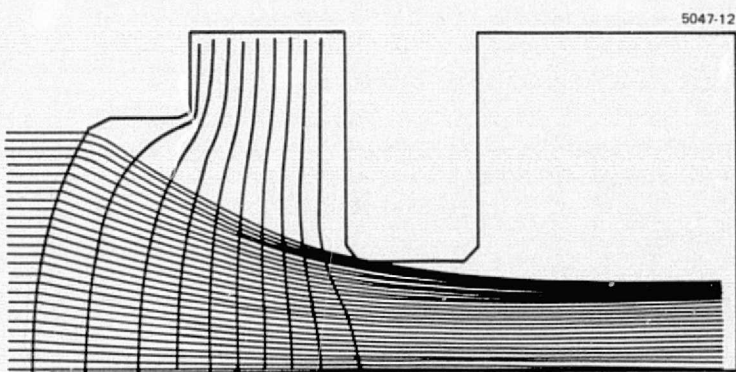




a)  $D_{ACCEL} = 0.152 \text{ CM}$



b)  $D_{ACCEL} = 0.103 \text{ CM}$



c)  $D_{ACCEL} = 0.081 \text{ CM}$

Figure 18. Ion beam trajectories computed for variations in accelerator grid aperture diameter.

Table VI. Parameters for Low Transmission Accelerator  
Grid Ion Optical System Design

Screen Grid	in.	cm
Thickness	0.015	0.038
Aperture Diameter	0.075	0.191
Aperture Spacing	0.087	0.221
Reduction in Spacing Pattern, %		0.4
Open Area, %		67.6
Accelerator Grid	in.	cm
Thickness	0.015	0.038
Aperture Diameter	0.040	0.102
Aperture Spacing	0.037	0.221
Open Area, %		19.2

T1872

### C. Experimental Results

Two approaches have been employed to reduce doubly-charged ion densities while still maintaining high total efficiency:

1. Parametric variations establish optimum operating conditions with minimum double ion content. This phase of testing was carried out in conjunction with the performance map described earlier.
2. Thruster geometry changes, in particular the ion optical system, were evaluated in order to establish optimum performance, again with minimum double ion content.

#### 1. Parametric Investigation

As the performance mapping of Section II has shown, the total thruster efficiency as a function of input power is relatively insensitive to the selection of control parameters. Thus, the percentage of doubly-charged ions should be weighed more heavily in the selection of these control parameters provided the necessary relationships are known. The performance mapping provided a range of

thruster operating conditions on which double ion studies could be based. The range of parameter selections were

$V_{DIS}$  35 to 41 V

$\epsilon_I$  185 to 250 eV/ion

$I_B$  0.5 to 2.75 A

$V_{NET}$  1100 to 1300 V

Selected points from the performance mapping of Task I are shown in Fig. 19 where the double ion current density ratio is plotted as a function of corrected mass efficiency. The solid line represents the data points which would be obtained by varying the beam current at a discharge voltage of 37 V with discharge losses of 185 eV/ion. The data appear to have the following trends:

1. At a given beam current, any attempt to increase mass utilization efficiency by increasing the discharge voltage results in an increase in the doubly-charged ion ratio with little or no increase in the corrected mass efficiency. The same appears to be true, to a certain extent, with respect to discharge current, however, the results are not so clearly defined.
2. The high efficiencies (beam currents) have a correspondingly higher percentage of doubly-charged ions.

The first of these observations can be explained on the basis of ionization cross-sections, while the latter needs further evaluation in terms of ion and neutral densities as predicted by beam current and neutral loss rate, respectively.

A linear dependence of the doubly-charged ratio on the ion density can be seen in Fig. 20 where neutral loss rate and the double ion ratio are both plotted as a function of beam current. For

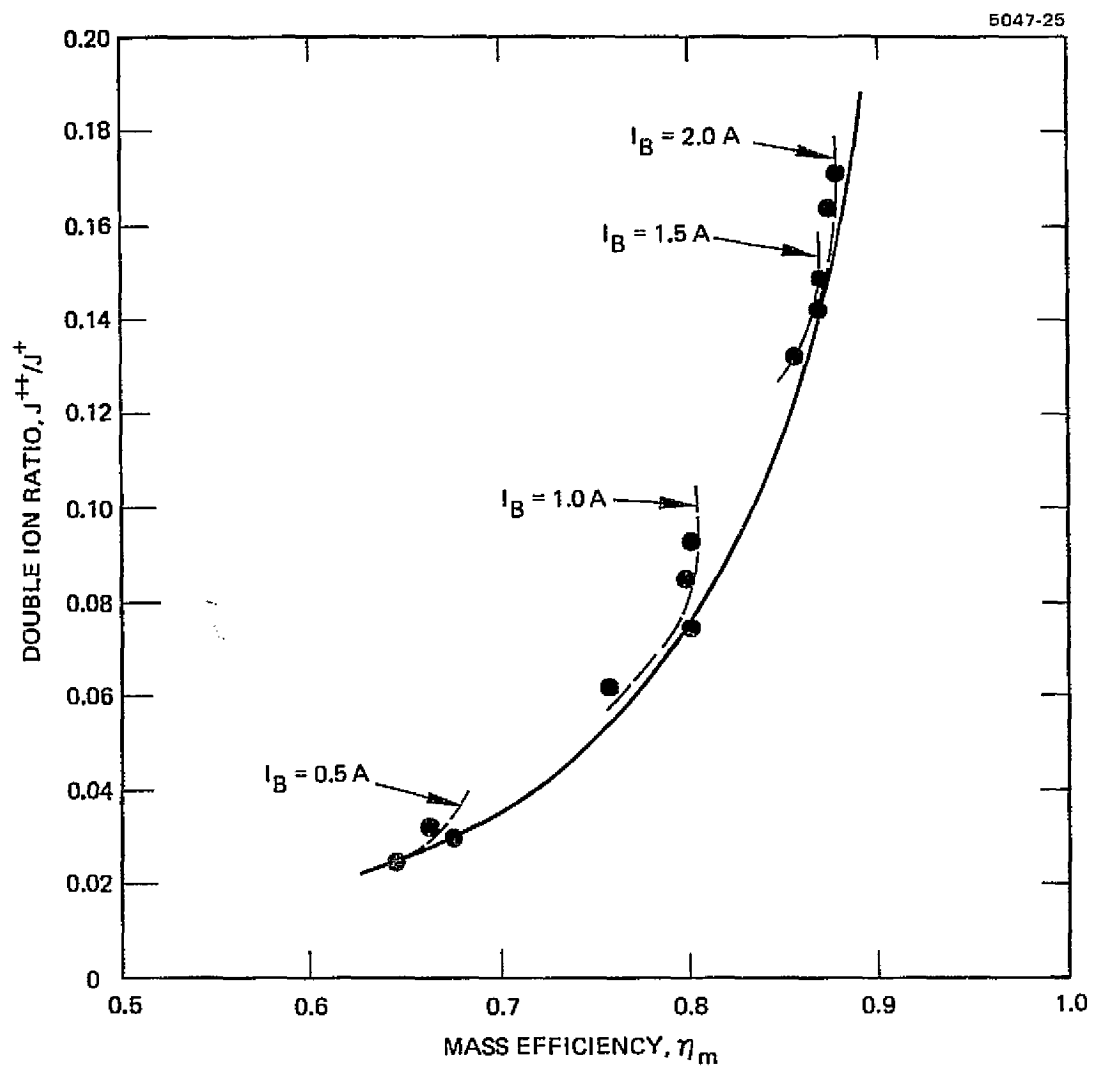


Figure 19. Performance map data relating the double ion ratio to discharge mass efficiency. Dashed lines indicate an increase in eV/ion at a given beam current.

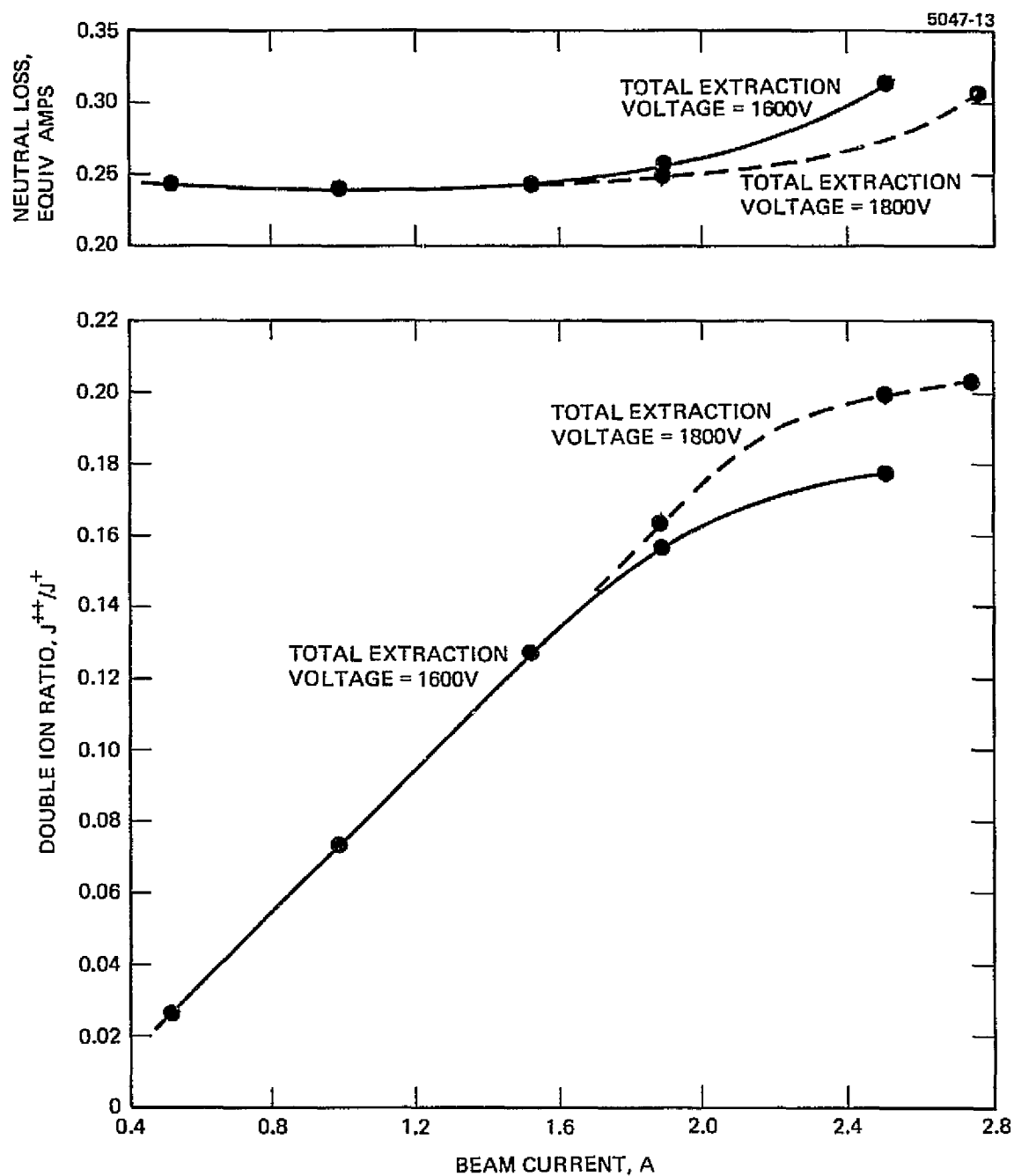


Figure 20. Double ion fraction and neutral loss rate as a function of beam current.  $V_D = 37$  V,  $\epsilon_I = 185$  eV/ion.

a thruster operating at maximum propellant utilization the neutral loss rate should be a constant regardless of total flow. This, in fact, was found to be the case. However, as the neutral loss rate remains constant, the double ion fraction increased in a linear fashion up to about 2.0 A beam current. At currents above 2.0 A the double ion ratio began to approach a constant value while the neutral loss rate started to increase. It was suspected that at these higher beam currents the thruster was operating near the limit of the ion optical system and as a result the mass utilization approached a constant value. This, in fact, was shown to be the case by raising the net accelerating voltage whereby both the mass utilization and double-ion ratio continued to increase while the neutral loss rate again approached a constant value. Therefore, at a given electron energy and neutral density the doubly-charged ion fraction will increase linearly with ion density.

If the double-ion production rate is a strong function of  $\eta_m$  based on the measured thruster values, i.e., beam current, neutral loss rate, etc., the same sort of relationships should be observed when analyzing the double-ion ratio as a function of thruster radius. This case is shown in Fig. 21 where  $J^{++}(r)/J^+(r)$  is plotted as a function of total ion current density, for beam currents ranging from 1.0 to 2.5 A. It is of interest to note that for any given thruster radial location the double-ion ratio increases linearly with ion density in much the same manner as it does for the thruster with total beam current. However, for constant ion current density the double-ion ratio decreases rapidly with increasing distance from the centerline. One explanation of this is that the neutral density may not be uniform across the discharge chamber, but increases with increasing radius. In order to further investigate the assumption of a radially increasing neutral density, the theoretical analysis of Masek<sup>10</sup> is used to predict a possible neutral density distribution. The analysis is based on a two-dimensional configuration, but since the optics boundary is being evaluated, only the solution at  $z = L$  is considered. The analysis

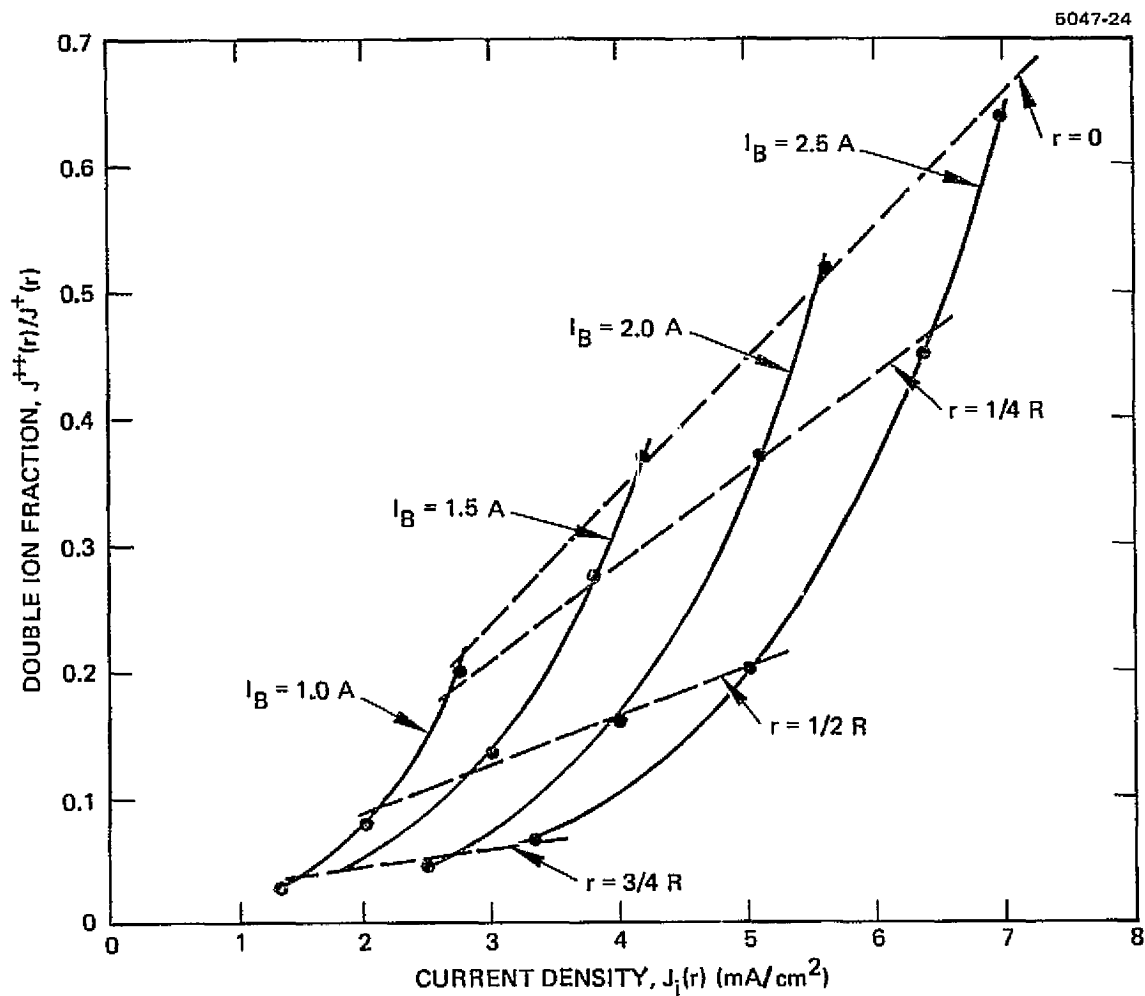


Figure 21. Double ion fraction as a function of radial current density.

predicts an exponential increase in neutral density with radius subject to the boundary condition of a known overall neutral loss rate. Once the neutral density at the various radial locations is known, it is then possible to calculate a radial mass efficiency,  $\eta_m(r)$ , based on the ion  $J_i(r)$ , and an equivalent neutral current density  $J_o(r)$ . The results are shown in Fig. 22 for the same data points shown in Fig. 21. As can be seen the curve is very similar to that of Fig. 19. Thus, although the above analysis is approximate, it does indicate that a very nonuniform neutral density distribution could exist, with results consistent with overall thruster operating conditions.

The results of the parametric study can be summarized briefly; the double ion ratio was found to be a strong function of the mass utilization efficiency, thus, total efficiency, and any gains which were made in improving thruster performance were also accompanied by an increase in the double ion concentration. This applied in a similar manner to the radial parameters and distributions.

## 2. Geometric Investigation

Since the ion and neutral densities are the parameters relating mass efficiency and double-charged ion ratio, some assumptions based on the preceding data can be made with respect to the accelerator grid open area. First, the neutral loss rate varies in direct proportion to the accelerator grid open area, and second, if the ion to neutral density ratio remains constant, then the double-to-single ion ratio will remain constant. The latter assumption is also constrained by the fact that the electron temperature and primary-to-maxwellian density ratio are not changing appreciably. Based on these assumptions it is possible to define a new mass efficiency

$$\eta'_m = \frac{I_B}{I_B + I_{o_{EM}} (\phi'/\phi_{EM})} \quad (6)$$



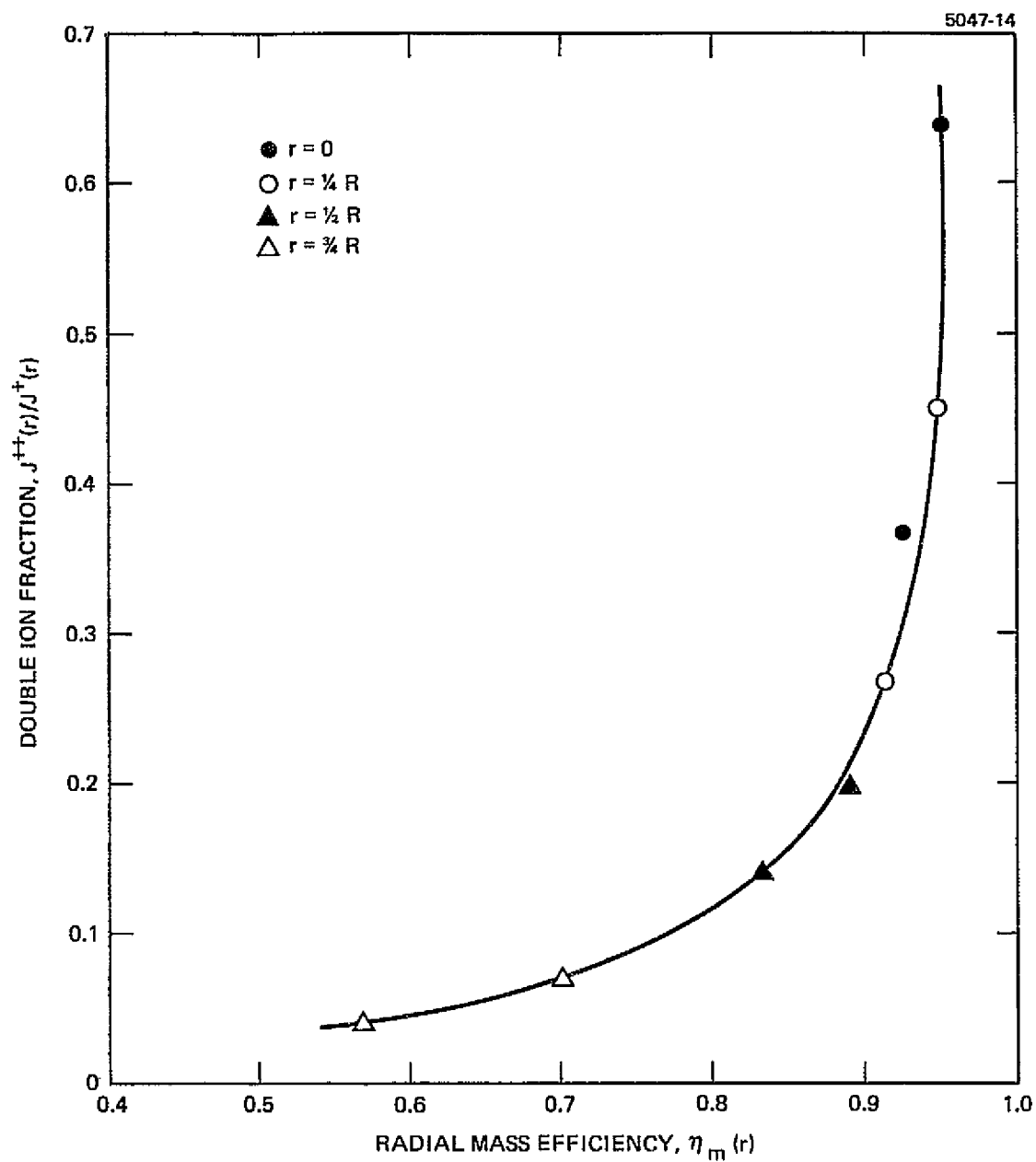


Figure 22. Double ion fraction as a function of mass efficiency for selected radial locations. Data points are for  $I_B = 1.5$  A and  $I_B = 2.5$  A.

where  $\phi'$  is the new accelerator grid open area fraction and  $I_{0EM}$  and  $\phi_{EM}$  are the neutral loss rate and accelerator grid open area fraction, respectively, for the EM optics. In addition to the SHAG optics described earlier in this section, a large hole accelerator grid (LHAG) set was also assembled to provide additional data on the effects of grid open area fractions and thruster performance. The LHAG optics were made simply by etching an EM accelerator grid until the desired aperture size was obtained. This also reduced the thickness, but not enough to appreciably affect the structural integrity. The final open area fraction achieved was approximately 60%. From eq. (6) an increase in mass efficiency should be realized with the use of SHAG optics, provided all the assumptions stated earlier are satisfied. Conversely, the LHAG were not expected to perform as well relative to EM standards.

Both sets of optics were evaluated with the results shown in Fig. 23. The discharge voltage in all cases was 37 V with discharge losses of 185 eV/ion. The mass utilization efficiency was varied by changing beam current and mass spectrometer scans were taken at each data point. As shown, a 2 to 3% gain in corrected mass efficiency can be realized with the use of SHAG optics. However, if one is willing to sacrifice part or all of this gain by operation at reduced discharge voltage, then a significant reduction in double ion content can be achieved. This is shown in Fig. 24 where the double ion ratio is plotted as a function of total, rather than mass, efficiency. By lowering the discharge voltage to 30 V, a 50% reduction in the doubly-charged ion current can be achieved while still maintaining the EM design criteria of 70 to 72% total thruster efficiency. Also shown are data points for 35 V discharge voltage.

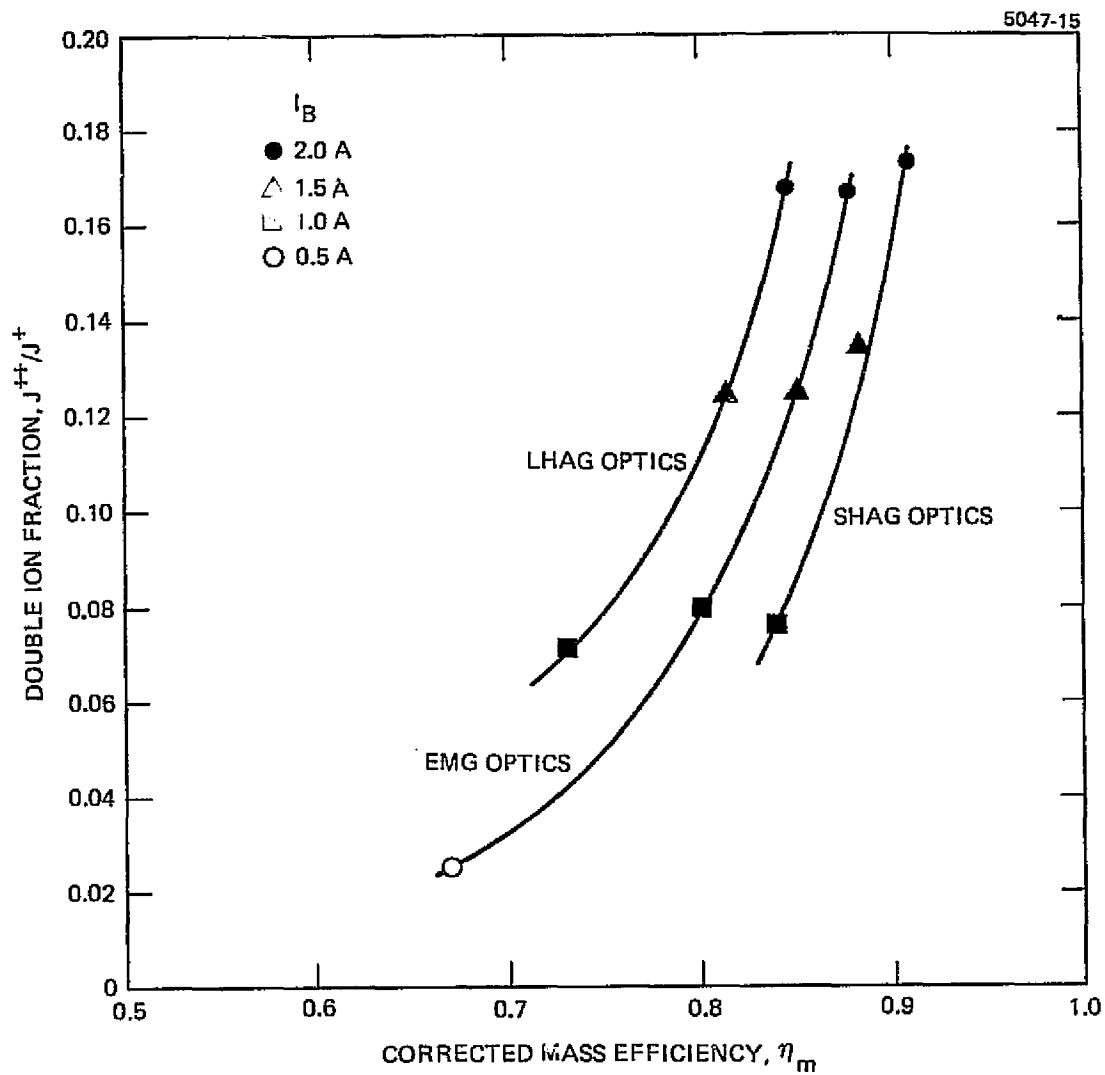


Figure 23. Double ion fraction as a function of mass efficiency for three different accelerator grids.  $V_D = 37$ ,  $\epsilon_I = 185$  eV/ion.

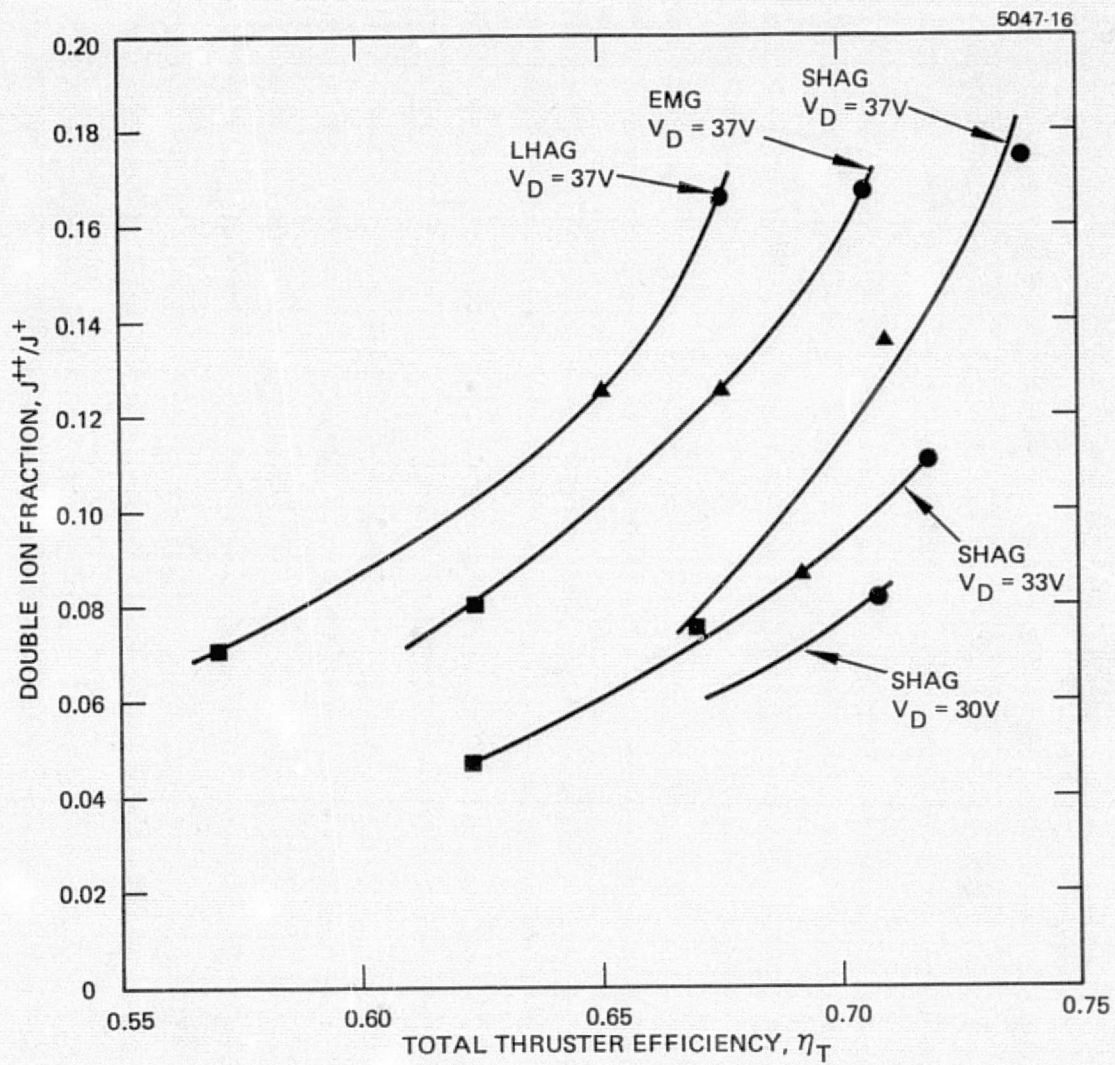


Figure 24. Double ion fraction as a function of total thruster efficiency.

#### IV. THRUSTER POWER CONDITIONER INTERACTIONS

The interaction between the thruster and the individual power supplies of the power processor unit (PPU) needed for its operation can significantly affect the capability of either or both to meet the exacting specifications that are necessary to make an ion thruster system an attractive alternative to other forms of space propulsion. The goal of this portion of the program has been to explore methods for minimizing the impact of thruster operating characteristics on the power processor requirements that are necessary to establish a stable, reliable system. Additionally, several techniques have been explored for reducing the number of power supplies necessary to operate the thruster. The following sections describe the work done towards accomplishing these goals.

##### A. Discharge Current/Voltage Oscillations

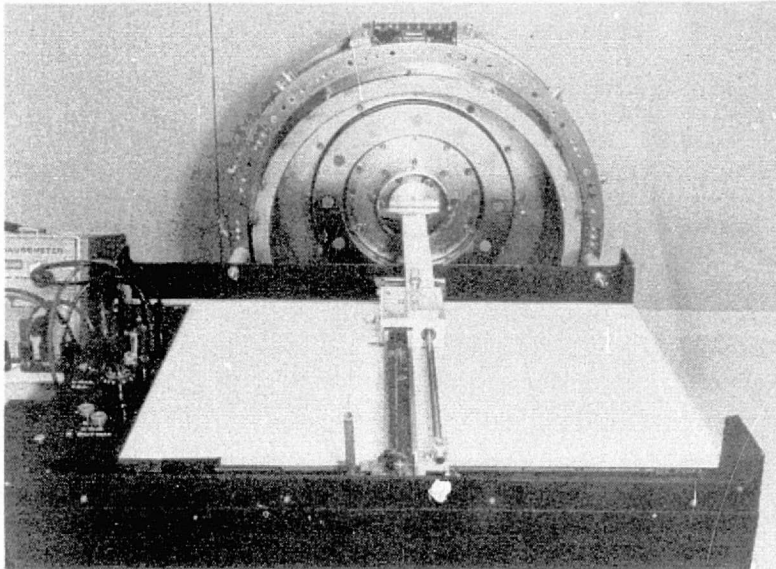
As discussed in Section II, relatively high frequency (10 to 20 kHz) oscillations are observed in the discharge voltage or current, dependent on the discharge power supply output. The onset and frequency of these oscillations is more or less independent of the power supply used, but can be related to certain thruster parameters. It was thought initially, that it might be possible to find a means of modifying the thruster design to eliminate these oscillations. Small variations in several parameters produced changes in frequency of the oscillations and/or onset conditions but no real progress was made in defining a reliable method of reducing or eliminating these oscillations. Parameters that were observed to influence onset, amplitude, and frequency of discharge voltage/current oscillations were:

- Magnetic baffle coil ampere-turns
- Cathode propellant flow rate
- Baffle support geometry
- Baffle diameter

All of these parameters suggest that these oscillations are a result of some form of current driven instability in the cathode plasma. Two types of oscillation were observed. One is characterized by high frequency oscillation with a relatively stable period and primarily affects the discharge current or voltage. The other is a low frequency (50 to 500 Hz) oscillation that is essentially a relaxation oscillation between two discharge modes. The low frequency oscillation affects both the beam current and voltage and consequently the entire power processor. This low frequency oscillation can be damped and essentially eliminated by increasing the magnetic baffle coil ampere turns. These conditions were known at the outset of this program and therefore the first experiments performed here constituted an attempt to find a physical basis for this phenomena.

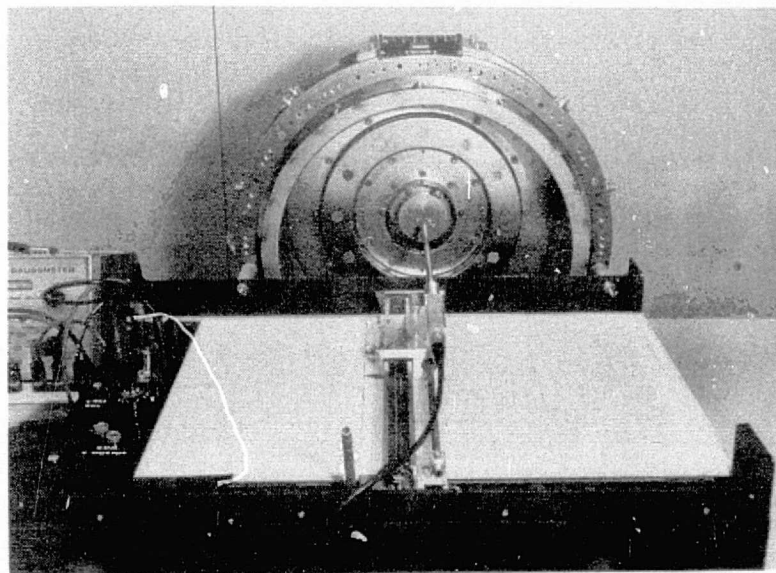
Precise measurements of the magnetic field distribution in and around the cathode polepiece were made using the precision gaussmeter probe positioner shown in Fig. 25. The magnetic baffle current was varied and the changes in field distributions were measured and analyzed. Figures 26 and 27 show the differences in axial and radial magnetic field components for selected locations in thruster S/N 301-B (representative of the 700/800 series Engineering Model Thruster). The most stable operating points for this thruster are obtained with a magnetic baffle current of 3.5 A (10.5 turn baffle coil). This means that the discharge is not subject to "mode shifting" and the high frequency (18 to 20 kHz) oscillation amplitude is near its minimum value. Note that for this baffle current, the axial magnetic field strength goes through zero and reverses direction on the axis, inside the pole piece, at a point just downstream of the cathode orifice (distance  $\sim 3$  mm). This measurement was obtained with a hole in the baffle. Similar axial field measurements were made using the thruster that had exhibited efficient, relatively oscillation free operation during the preceding program (NAS 3-16949) and these measurements are shown as Fig. 28. The baffle current required to produce this quiescent operation was 4.5 A

M10530



a

M10531



b

Figure 25. Magnetic field plotting apparatus. (a) With alignment fixture. (b) With Gaussmeter probe in place.

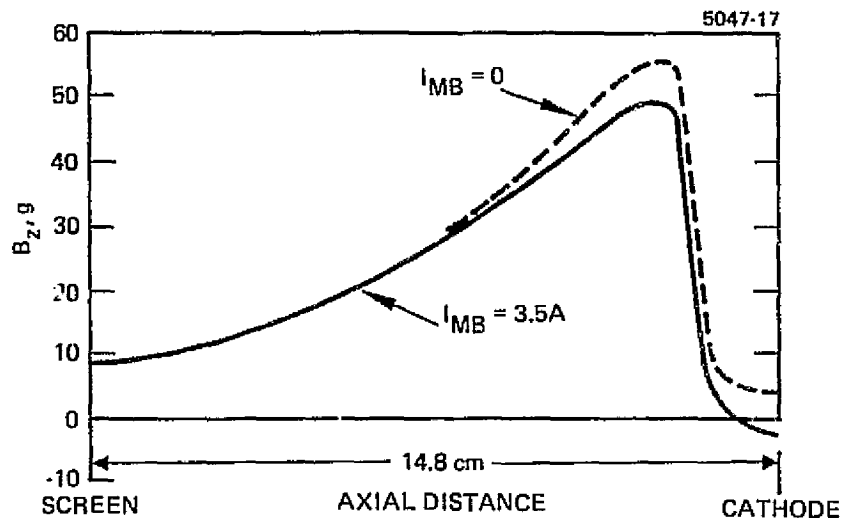


Figure 26. Variation in axial magnetic field component,  $B_z$ , on the thruster axis (Thruster S/N301-B) with and without magnetic baffle current.

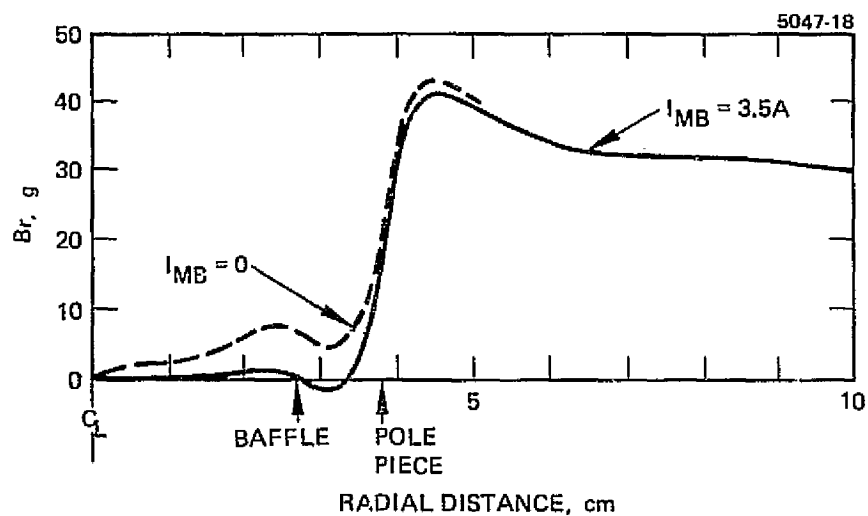


Figure 27. Variation in radial magnetic field along a radius in the plane of the baffle, with and without magnetic baffle current.



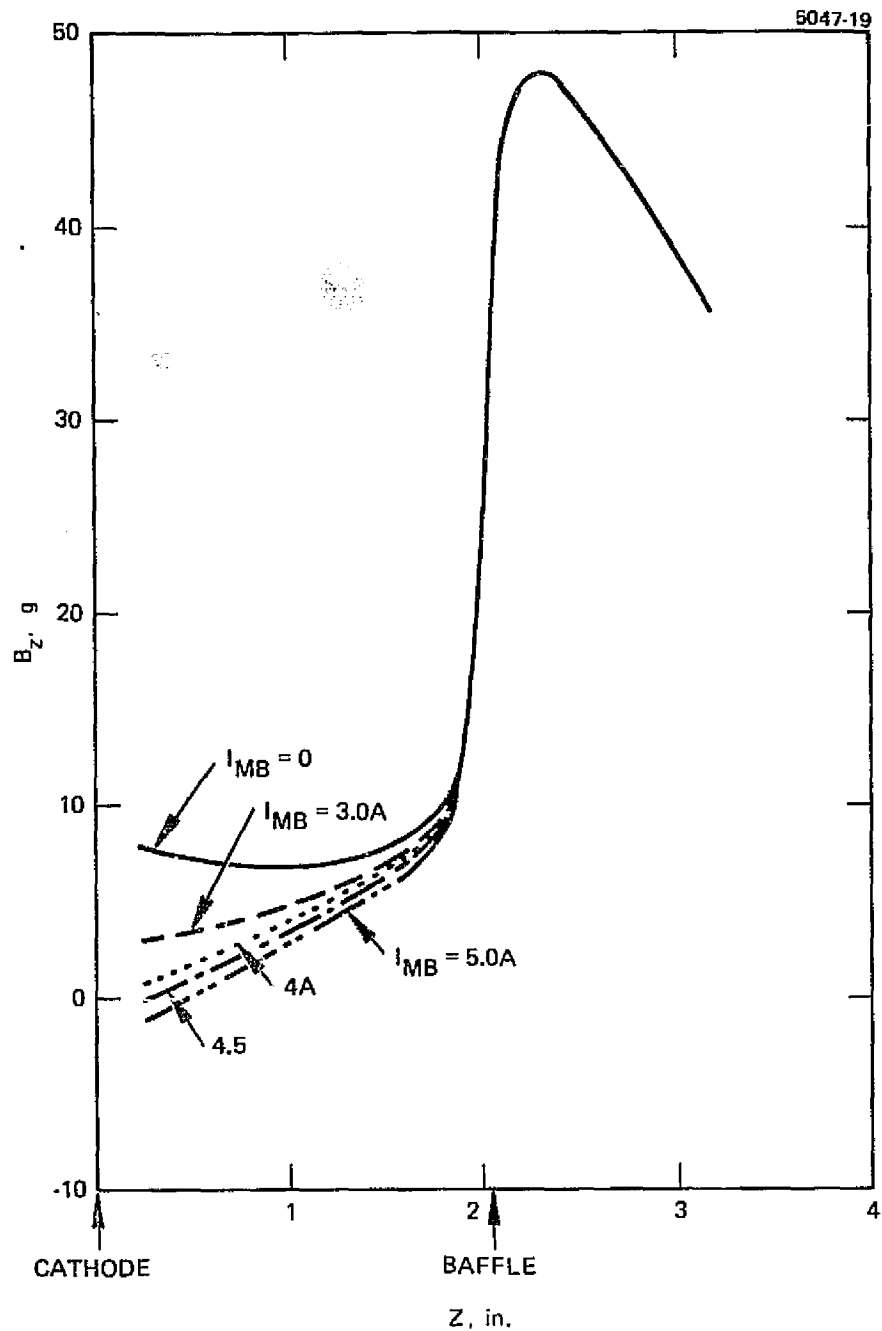
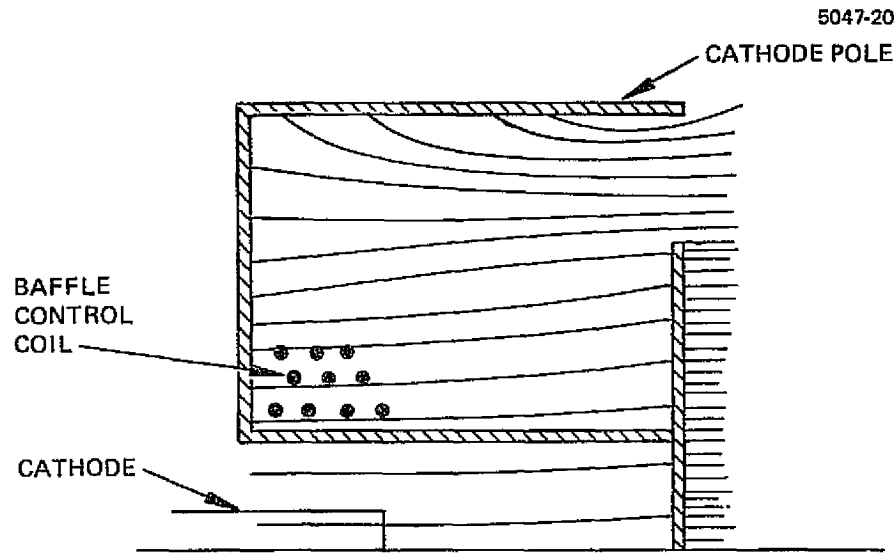


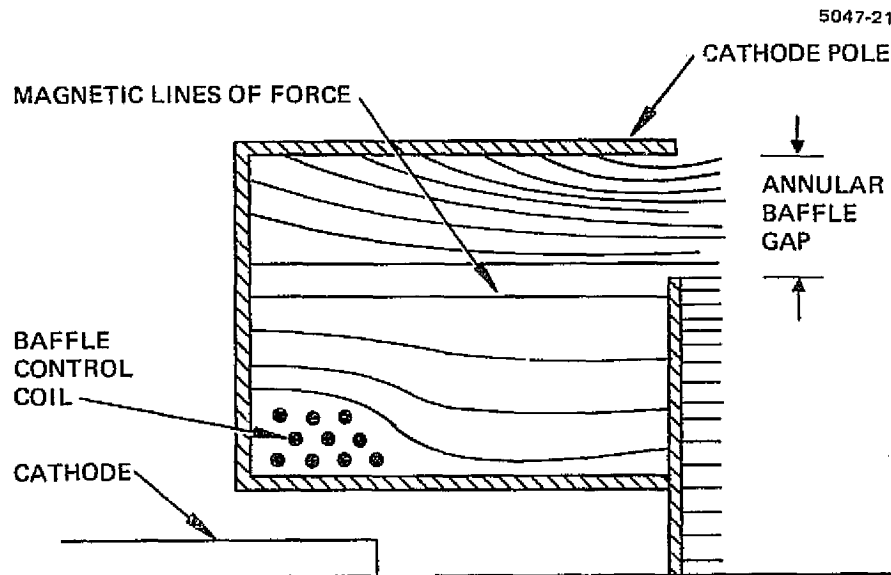
Figure 28. Axial magnetic field variation on the discharge axis near the cathode orifice with magnetic baffle current as a parameter (experimental thruster).

or greater, and 4.8 A was the point most frequently run. Note that this provides the same kind of axial field condition in the vicinity of the cathode orifice as existed in the case for S/N 301-B, shown in Fig. 26. By cutting a slot in the baffle, extensive probe measurements were made in the interior of the cathode polepiece in an attempt to carefully document the magnetic field conditions thought to be necessary for oscillation free operation. Using these field component data, a qualitative description was prepared to compare the distribution in magnetic field strength and direction in the region between the cathode and the main discharge chamber for values of magnetic baffle current above and below the "critical" value. This comparison is shown in Fig. 29 with the density of lines of force meant to portray field strength. Some effort was spent to make this description more quantitative, but it was discovered that the slot in the baffle altered the field distribution around the annulus region between the baffle and polepiece and perhaps in the entire interior. For this thruster, the HRL experimental electromagnet thruster, hysteresis was also observed in these magnetic field measurements after repeated variations of magnetic baffle current and consequently this approach to investigating thruster discharge oscillations was abandoned. Moreover, the cathode propellant flow rates for which low oscillation conditions are observed tend to fall within a relatively narrow range of values and it is uncertain as to which parameter is more important (since they are not independent). Since no really adverse effects could be attributed to the operation of a thruster discharge chamber that exhibits discharge current/voltage oscillations on the basis of the performance mapping discussed earlier, the search for a means of reducing or eliminating this phenomena was terminated at this point.

Here again, as under the previous program, it is concluded that several parameters control the transport of electrons within the cathode pole region and thereby control the discharge "impedance." Several combinations of these parameters may establish electron transport to define a discharge "mode" and these parameter combinations may



a)  $I_{MB} = 0$ , RADIAL FIELD COMPONENT IN THE ANNULAR BAFFLE GAP IS IN THE POSITIVE R DIRECTION



b)  $I_{MB} > I_{CRITICAL}$ , RADIAL FIELD COMPONENT IN THE ANNULAR BAFFLE GAP REGION REVERSES, AXIAL FIELD STRENGTH ON THE AXIS IS GREATLY REDUCED AND PASSES THROUGH ZERO NEAR THE CATHODE ORIFICE.

Figure 29. Illustration showing effect of magnetic baffle control current on the field distribution within the cathode polepiece. Distribution deduced from measurements like those shown in Figs. 2 and 4.

not differ greatly. Thus it is possible to establish conditions so that relaxation oscillations between "modes" occur or that an oscillatory behavior is inherent in the electron transport process, or both. To eliminate oscillatory behavior consequently is thought to require a truly independent means of controlling hollow cathode emission, which may or may not be possible.

B. Beam and Accelerator Power Supply Requirements

The goal of this project was to determine the feasibility of simplifying thruster control by incorporating fast current limiting in the beam or screen power supply as an alternative to the high voltage turn-off and recycle sequence that was in use at the time of this investigation. A secondary objective was to evaluate the feasibility of combining the accelerator power supply with the screen (beam) power supply. The investigation began by mapping the voltage-current requirements that exist in thruster operation for screen voltages between the off and run levels. The experiments performed indicated that current limiting alone cannot prevent the thruster from operating in low voltage, high impingement current regions unless the discharge current is reduced. The requirement for discharge current reduction to restore high voltage in the screen and accelerator supply is equivalent to a recycle sequence and consequently the use of fast current limiting has no real advantage over the use of overcurrent initiated high voltage shutoff. Moreover, the ion optics assembly sustained damage in the "out of perveance" operation that was permitted in the experiments performed to map the voltage-current characteristics and some amount of detrimental operation of this sort can be anticipated with a current limiting system. This hazard to the ion optics assembly can be reduced by improving the response of the control loops, which also improve the dynamic response to load oscillations, etc. A preliminary control loop analysis was performed that indicated that a wide bandwidth power supply may be practical using lead compensation, but its main advantage

would be in dynamic output voltage regulation rather than in overcurrent protection by current limiting or high voltage shutoff. Investigation of the combined screen and accelerator power supply concept was more rewarding.

Many four-trace oscilloscope photographs of  $V_s$ ,  $V_a$ ,  $I_s$ ,  $I_a$  transient events were collected with a variety of HV supply configurations using the HRL console screen supply and a wide bandwidth programmable KEPCO accel supply including:

1. Screen supply step at 0 accel voltage at various discharge currents
2. Screen supply step with various accel ramp up rates at various discharge currents
3. Accel supply slaved directly to screen supply at screen supply step and screen supply ramp up at various discharge currents and various screen-accel voltage ratios
4. Accel supply step at 0 screen voltage at various discharge currents
5. Dummy load characteristics of the above configurations.

Conclusions reached from these experiments are:

1. The screen and accel current, thruster transient response is essentially instantaneous. Screen and accel current can be defined by the instantaneous screen and accel voltage.
2. A dual winding HV supply will work with the present thruster design. High voltage application can be achieved under a variety of conditions using a slaved power supply arrangement, including a  $V_{scrn}$  to  $V_{accel}$  ratio of only 100 V to 125 V and from a discharge current of 2 A. In all cases the KEPCO accel supply current limit value was set for 100 mA, realistic for a flight design. In fact, this master-slave power supply configuration seems more desirable than independent power supply configurations since all intermediate HV operating points between HV off and HV fully on were observed to be very stable at discharge currents of 2 A or less. The

HV could be turned up very slowly with no intermediate instabilities or trips. Naturally one would like to establish a regime of operating points defining the path from thruster off to thruster on where each point on the path is unconditionally stable. Unstable regions were observed when increasing the discharge current after the HV is already established. Engineering Model thrusters of the 700/800 series have a tendency to oscillate at discharge currents in the range of approximately 4 to 6 A with accompanying overload trips. Closer inspection revealed that these trips result from the relatively low frequency discharge oscillations ( $\sim 200$  Hz) interacting with the screen supply output filter causing instantaneous excursions of screen voltage which, from conclusion 1, is known to be sufficient to drive the thruster out of perveance causing a trip. This phenomena is known to be improved by additional capacitive filtering in the screen supply. The recommendation is that the screen supply be respecified for increased filtering.

3. The backstreaming characteristic of the screen to neutralizer current path seems to be (a) monotonic, (b) have a definite upper limit of approximately 9 A, and (c) behave somewhat like a space charge limited diode and finally like a temperature limited diode at 9 A.

In summary, the only recommendation that can be made concerning specification of the screen and accelerator power supply based on this investigation is that the accelerator and screen supply can be combined (or outputs controlled) by a single control, and the frequency response of the output voltage regulation should be improved to at least 500 Hz.

#### C. Utilization of Discharge Power Supply for Auxiliary Functions

The discharge power supply has the capacity to deliver more than 400 W of power and could provide power for at least two auxiliary functions that now require separate power supplies. The cathode tip and isolator heaters are required only for thruster startup or at very low operating power levels. If it is not necessary to operate at low power levels for extended time periods, then the discharge power

supply could be used to supply the preheat function and thereby eliminate the requirement for at least two power supplies. The low voltage section of the cathode keeper power supply is another candidate for elimination. The output of this power supply is not usually varied during normal operation, and its function may be satisfied by tapping off the desired keeper discharge current with a dropping resistor connected to the anode lead. Again, some flexibility in thruster operation is lost, and the power dissipated in the resistor represents a loss, but the elimination of the weight and complexity of an extra power supply could be sufficient justification to warrant this modification.

#### 1. Evaluation of Concepts

The initial experiments performed under this project were planned to demonstrate feasibility of the concept, with minimal thruster heater modifications and the emphasis was placed on the circuitry for control of the discharge supply. A heater was installed on the thruster backplate to simulate the isolator heaters and the discharge power supply was connected to the thruster as shown in Fig. 30. Automatic control algorithms were implemented to operate the heater relay, discharge setpoint control and cathode keeper high voltage supply as described in Table VII.

The control algorithm chosen for the relay is very simple — being a function only of sensed cathode keeper current. During the thruster warmup period the relay is closed and the discharge supply is turned on providing power to the series heaters. During this period the sensed  $I_D$  (in the discharge return leg) and  $V_D$  accurately describe total heater power. In addition, a clamp circuit is implemented in the discharge current setpoint control circuit to automatically limit the discharge current to an adjustable predetermined level when the relay is closed. This provides a fail-safe means of protecting the heater from accidental burn-out and a very simple automatic start up algorithm for the discharge supply (i.e., the discharge supply is always on and commanded for the run setpoint).

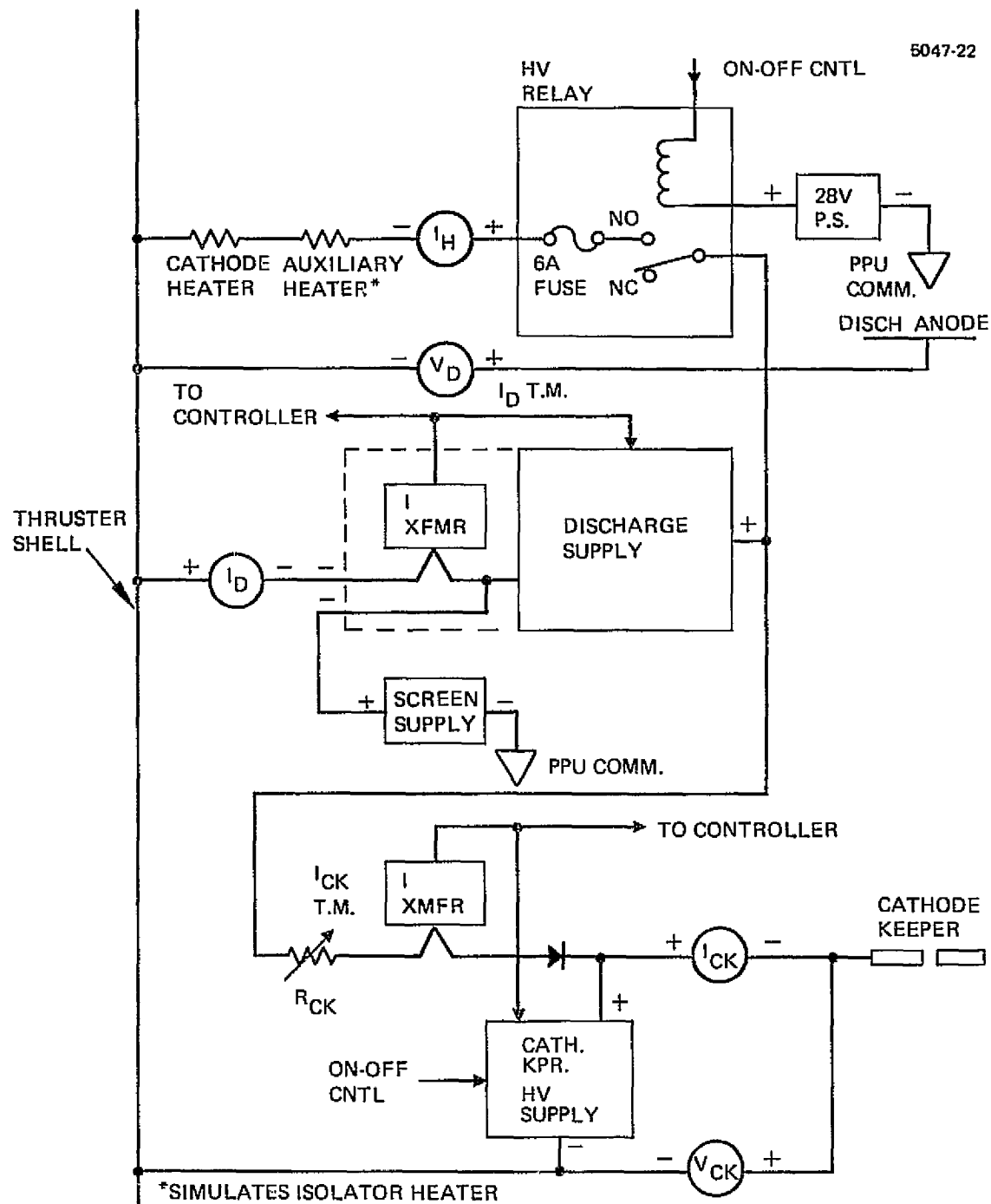


Figure 30. Shared discharge supply wiring diagram.



Table VII. Shared Discharge Supply Control Functions

Function	Condition
Heater relay on Heater relay off	$I_{CK}^{T.M.} \leq 100 \text{ mA}$ $I_{CK}^{T.M.} > 100 \text{ mA}$
Cathode keeper HV supply on Cathode keeper HV supply off	CK commanded on and $I_{CK}^{T.M.} \leq 100 \text{ mA}$ CK commanded off or $I_{CK}^{T.M.} > 100 \text{ mA}$
Discharge $I_{sp}$ control clamped 5 A Discharge $I_{sp}$ control unaffected	$I_{CK}^{T.M.} \leq 100 \text{ mA}$ $I_{CK}^{T.M.} > 100 \text{ mA}$

T1873

At the appropriate time vaporizer power and cathode keeper high voltage are turned on (based on automatic control functions already existing in the PPU test console). When keeper ignition occurs the relay drops out. Presumably, the discharge also ignites and arrives at the run setpoint ( $V_D = 37 \text{ V}$   $I_D = 10 \text{ A}$ ).

The relay control algorithm was arrived at by consideration of all possible states as listed in Table VIII. States 1, 2, 3, 4 have no significance and state 7 is presumed to be impossible since with discharge ignition both low voltage (via the dropping resistor) and high voltage are applied to the keeper. For the keeper to fail to ignite under these conditions would undoubtedly require a failure in the thruster. State 5 and state 8 provide the desired states of the relay and require no further discussion. State 6, however, requires heater power off in which case the cathode keeper will soon starve and return to state 5 which, presuming proper flow conditions, leads to state 8. In order to generate a 1 in state 6 (heater power applied) requires additional

Table VIII. Heater Relay Logic States

State	Discharge on Command	Discharge Lit	CK lit	Relay Closed
1	0	0	0	X don't care
2	0	0	1	X impossible
3	0	1	0	X impossible
4	0	1	1	X impossible
5	1	0	0	1
6	1	0	1	if 1 - O.K. htrs. on X if 0 - Ck will starve and go to state 5
7	1	1	0	X impossible
8	1	1	1	0

T1874

current sensing in the discharge anode which does not presently exist. Otherwise, if one simply bases the decision on sensed  $I_D$  in the return leg (where it presently exists) a race will occur in the table between state 6 and state 8 because sensed  $I_D$  includes heater current.

Finally, the logic for the cathode keeper HV section is shown for illustration only and required no modification.

A goal of this experiment was to implement the switching and control circuitry in a flight qualifiable manner. The system as shown impacts the PPU in the following areas:

1. Addition of cathode keeper dropping resistor
2. Modification to discharge supply current set-point low voltage control logic
3. Modification of sensed discharge current telemetry to the extent that true discharge current is the difference between sensed  $I_D$  and sensed  $I_{CK}$  (note that heater current and discharge plasma current are always mutually time exclusive)

4. Addition of heater switch element and drive circuitry
5. Addition of low voltage heater switch control logic.

It is apparent that 2, 3, and 5 are of no particular concern with respect to flight system design. The addition of the dropping resistor is also of no particular concern, since for the idea to be valid the resistor must have very modest power dissipation (e.g.,  $100\ \Omega$  at  $300\ \text{mA} = 9\ \text{W}$ ). Finally, selection of a switch element to implement the dc power transfer lead to consideration of two practical choices: (1) a relay, and (2) a series pass transistor. Although use of a transistor circuit would, in general, have certain difficulties associated with the requirement for isolated base drives and the physical mounting considerations associated with voltage isolation and power dissipation, for some types of missions it may be the best choice. A relay was chosen for expediency and as a representative example of a flight qualifiable circuit. In a flight system one would expect the stresses on the relay to be rather modest in view of the expected number of operating cycles and load characteristics of the heaters (mostly resistive). The relay used is a Kilovac model HC-1/S43 miniature vacuum relay capable of hot switching 18 A and has been used in the 8 cm TVBB program (NAS 3-17780). The power source for the relay coil is assumed to be derivable from housekeeping supplies in the PPU and poses no particular design problems or penalties.

Initial experiments were performed by waiting until isolator temperature had reached  $150^{\circ}\text{C}$  before initiating vaporizer power. The preheat time required for these experiments was on the order of 1 hour because the heater current was limited to 5 A by the cathode tip heater, and the auxiliary heater was not optimum for heating the thruster propellant feed system. Cathode keeper ignition was readily obtained using the keeper power supply high voltage section and a value of  $100\ \Omega$  for the dropping resistor,  $R_{ck}$ . Oscilloscope waveforms of the keeper current ignition and steady-state characteristics showed excellent, well behaved operation. The keeper was intentionally extinguished more than a hundred times followed in each case by successful automatic recycling of heater power and keeper discharge

ignition. In addition, many attempts were made to cause loss of keeper ignition (while running at  $I_{CK} = 200$  mA from  $R_{CK} = 150 \Omega$ ) by inducing various types of high voltage overloads including screen or accel off, screen or accel short circuit and screen to accel short from  $I_B - 2$  A steady-state operation. The only loss of keeper and discharge ignition observed was for the transient condition with beam (screen) voltage on and accel voltage off. Since this is not a normal condition and could not be tolerated because of possible ion optics or neutralizer damage, the use of the resistor tap on the anode voltage is considered to be a feasible alternative to the low voltage power supply now used for steady-state keeper operation. Some further experiments were performed to determine the limiting value of resistance that can provide this function for both start and run conditions. The results showed that:

1. Reliable, repeatable discharge ignition can be forced to occur at vaporizer temperatures representing modest flow rates at cathode keeper current less than 200 mA. For example, discharge ignition occurred at  $\dot{m}_c = 80$  mA eq. and  $\dot{m}_m = 1$  A eq. at  $I_{CR} = 105$  mA.
2. Once ignited cathode keeper ignition is maintained down to less than 20 mA keeper current over the range of test conditions including  $\dot{m}_c = \sim 0$  and  $\dot{m}_m = \sim 0$  ( $T_{CV} = 242^\circ\text{C}$  and  $T_{MV} = 243^\circ\text{C}$ )
3. The maximum value of the dropping resistor for reliable discharge ignition is roughly 150 ( $I_{ck} = 200$  mA), representing about a 6 W power loss.
4. Reignition of the keeper and discharge after switching the discharge and h.v. keeper power supplies off and back on again could not be demonstrated with the 1000 volt high voltage section of the keeper power supply. Reignition always required in addition switching on the heater and required a relatively random time period under the start conditions.

Thus these preliminary experiments have shown that the concept of the switched heater circuit is definitely feasible and will likely lead to a much faster warm up sequence and simpler and lighter PPU configuration where mission requirements allow mutually exclusive

operation of discharge and heaters. To realize the faster warm up sequence, a modification of thruster heater will be required so that the full discharge power can be utilized. The following section describes results obtained with one method of implementing this heater modification. Elimination of the low voltage section of cathode keeper power supply is also feasible and thus a high voltage pulsed igniter to supply ignition also appears more feasible.

## 2. Rapid Start-Up Experiments

To demonstrate the feasibility of using the discharge supply to rapidly heat the thruster it was first necessary to add a new heater and modify an existing heater. The new heater was attached to the discharge chamber side of the inner wall of the propellant plenum. The size of this heater was selected to match the nominal hot resistance of the cathode tip heater. The heater modification consisted of detaching the end of the cathode isolator heater which is normally connected to the thruster shell so that the cathode isolator heater and cathode tip heater could be connected in series. This combination was operated in parallel with the series combination of the plenum heater and main isolator heater as shown in Fig. 31.

Initially, the test setup was configured as shown in Fig. 30. However, while checking the operation of the control logic with the discharge supply connected to a carbon pile resistor in place of the thruster heaters the high voltage relay being used failed. It was then decided the basic objective of demonstrating feasibility could be achieved by using a separate dc supply switched to replace the discharge supply during the heating phase as shown in Fig. 31. The power processor was also modified to replace the low voltage section of the keeper supply with the discharge supply as shown in Fig. 31.

The operational sequence employed for the rapid start-up tests was (1) preheat thruster with commercial dc supply (in lieu of the discharge supply), (2) apply cathode vaporizer and main vaporizer power when cathode vaporizer temperature reached approximately  $100^{\circ}\text{C}$ , (3) periodically apply cathode keeper voltage until keeper ignition, and (4) periodically apply discharge voltage until discharge ignition. The

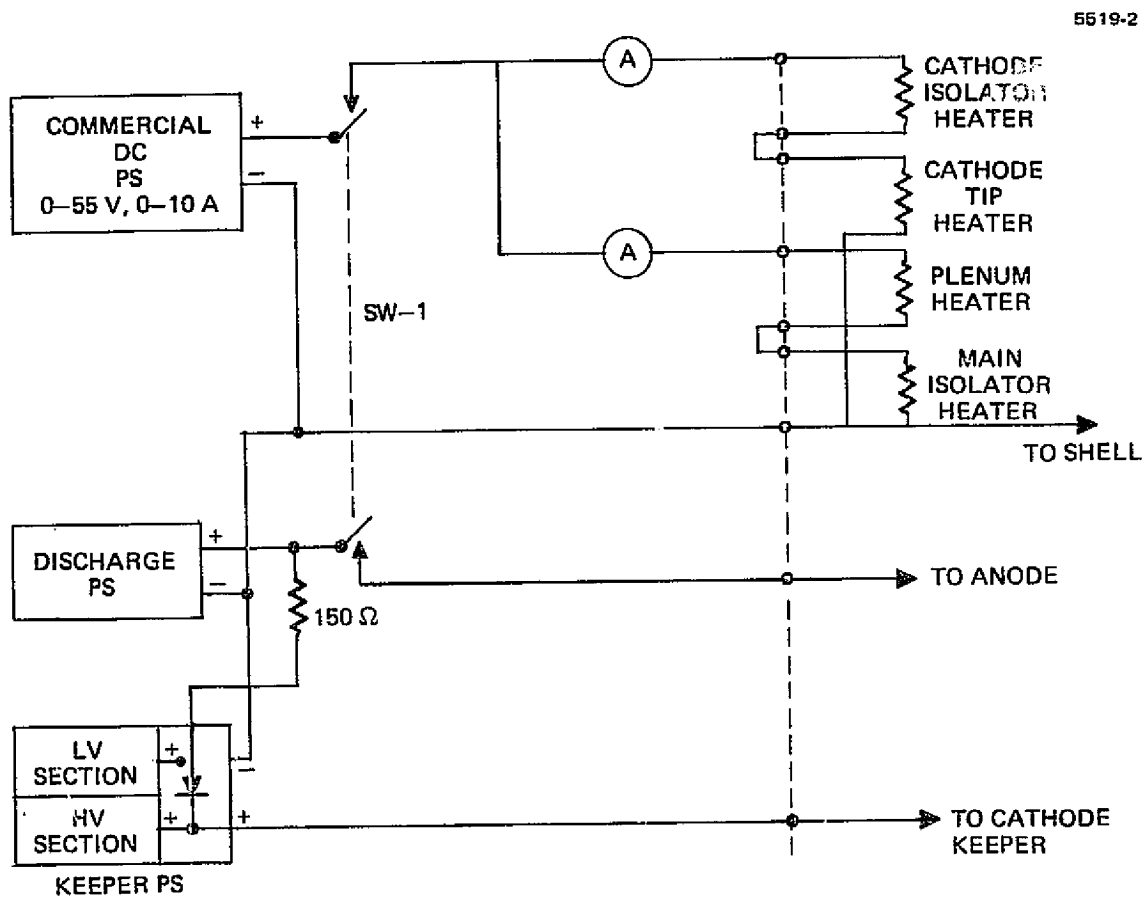


Figure 31. Rapid start-up experiment wiring diagram.

power to the isolator, cathode tip, and plenum heaters was removed whenever discharge voltage was applied to the anode (see Fig. 31).

For these tests the output of the dc heater supply was adjusted to limit the cathode tip (and cathode isolator) heater current to 4.5 A. At this setting the maximum voltage was 34 V, and 3.8 A was flowing through the main isolator and plenum heaters. The maximum total power to the four heaters was 282 W, well below the rating of the discharge supply for a 30 cm thruster.

With the sequence described above cathode ignition was achieved in 7.5 to 9 min, and discharge ignition was achieved 11 min after initial application of heater power. Temperature profiles at five locations on the thruster are presented in Fig. 32 for the first rapid start-up test. No effort was made to reduce the start-up time further by optimizing the amount of heater power or time of vaporizer power application. Keeper operation seemed to be unaffected by the substitution of the discharge supply for the low voltage section of the keeper supply.

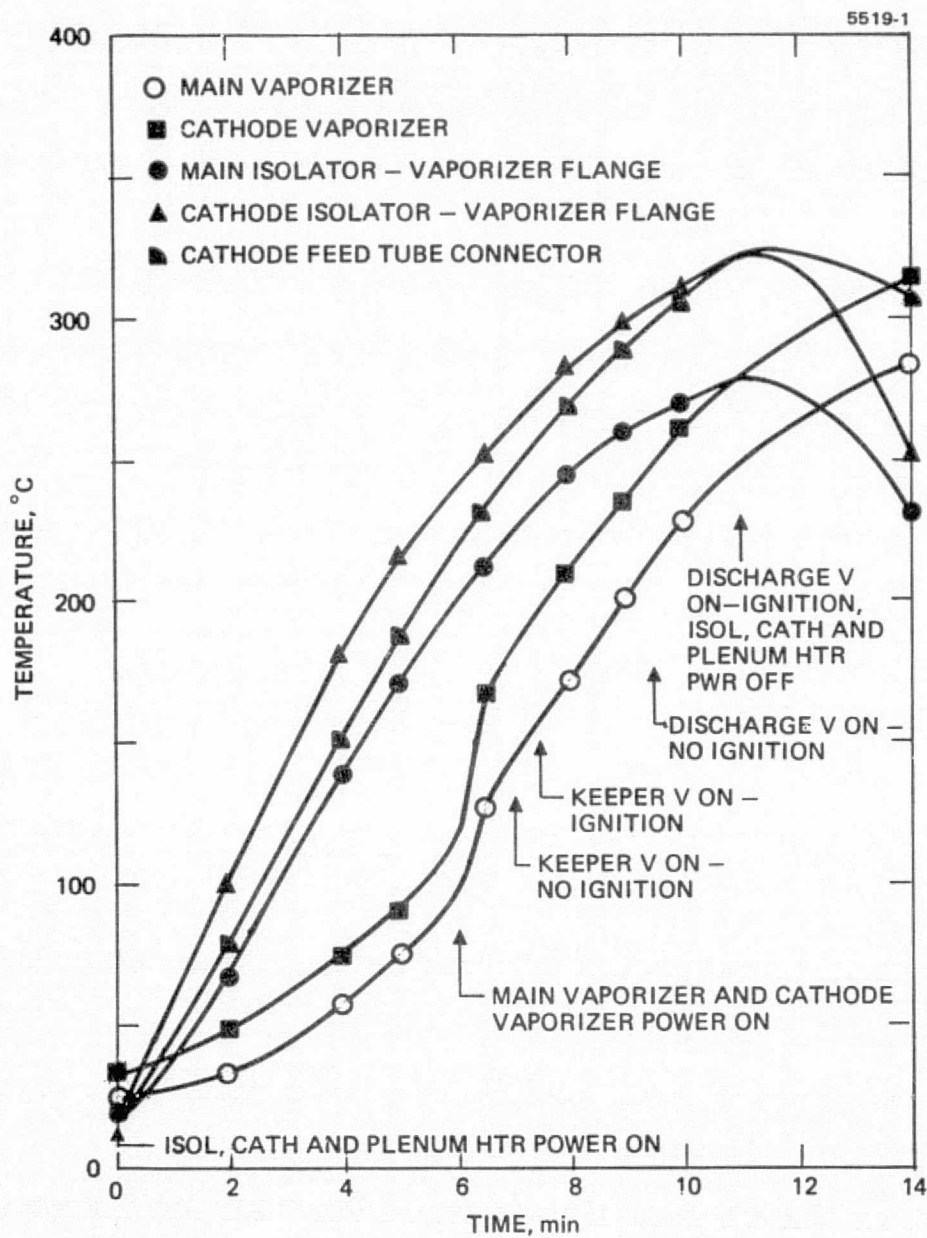


Figure 32. Thruster temperature profile during rapid start-up experiment.



## V. THRUSTER-GIMBAL SYSTEM ANALYSIS

Efforts under this task consisted primarily of (1) a survey of gimbal mechanisms which have been developed for thrust vector control (TVC) under other programs, and (2) the development of a computer program to calculate the resultant torques and forces for an arbitrarily orientated thruster array. The latter effort was an alternative to the original task of designing a specific gimbal actuator and was initiated with the concurrence of the NASA Program Manager.

### A. Survey of Gimbal Mechanisms for Thrust Vector Control

One of the most important factors in thruster array design is thrust vector control mechanization. The mechanization approach is highly dependent upon requirements such as thrust direction accuracy, coupling between the three torque axes, thrust loss, thruster particle (ions and atoms) flux distributions, reliability and the particular mission under consideration. For example, for planetary missions, cruise mode perturbations and biases are relatively small and thruster gimbal angles of 5 to  $10^\circ$  provide sufficient control authority. However, on out-bound type trajectories, the number of operating thrusters is gradually decreased. In order to maintain the thrust vector through the center-of-mass, additional gimbaling is required. Thus, the gimbal requirement for a planetary mission design must include the variable number of operating thrusters as well as control authority.

In the case of earth orbital (EO) missions, the number of operating thrusters is generally less variable since available power is relatively constant. (An exception to this condition occurs if orbit raising through the Van Allen Belt is considered.) However, the torque required for EO mission maneuvers (e.g., vehicle attitude changes of  $180^\circ$  twice per orbit) is one to two orders of magnitude greater than for planetary missions. The gimbal angles needed to produce such torques are generally in the range of 20 to  $30^\circ$  and thus result in significant thrust losses.

The first TVC hardware<sup>11</sup> developed was designed to minimize as many uncertainties as possible by use of a two axis array translator and single axis thruster gimbals. This approach provided relatively accurate knowledge of thrust vector pointing, good control authority, and minimized coupling between axes. Unfortunately, the translator single point failure possibilities, combined with its weight and complexity resulted in a search for alternatives.

Once the thrust vector accuracy requirements were relaxed and the elimination of single point failures were encouraged, the logical choice was individual thruster two axis gimbaling.

Workers at Jet Propulsion Laboratories (JPL) carried this design concept into a prototype hardware phase. The JPL concept, illustrated in Fig. 33, packages both gimbal actuators into a single housing (Fig. 34). To provide for launch vibration, a pyro-released latch is used to support the thruster free gimbal pad. The JPL overall packaging approach was selected to provide actuator thermal control, to prevent thruster heat rejection to the vehicle, and for thruster thermal control. Based on analytical studies, the open sides and slanted thermal blanket were believed to be necessary for thruster thermal control. The JPL "thrust assembly" designed for the Encke Flyby Mission<sup>12</sup> was estimated to weigh 91 kg, or 15.2 kg/thruster.

Recent studies of the Solar Electric Propulsion State (SEPS) by Rockwell International<sup>13</sup> and Boeing<sup>14</sup> for Marshall Space Flight Center, included thruster array conceptual design for up to twelve thrusters. For these studies, thruster array packaging constraints, thermal control limits, and interface definition were provided by Hughes Research Laboratories and NASA LeRC Research Center. The resulting designs were relatively strongly influenced by the results of tests performed by Mirtich and Rawlin of LeRC. In the LeRC tests, it was concluded that thrusters could be stored at temperatures down to -200°C, and that thruster operation was essentially unaffected by thermally insulated surrounding or by direct solar radiation up to 2.5 sun's intensity. Thus,

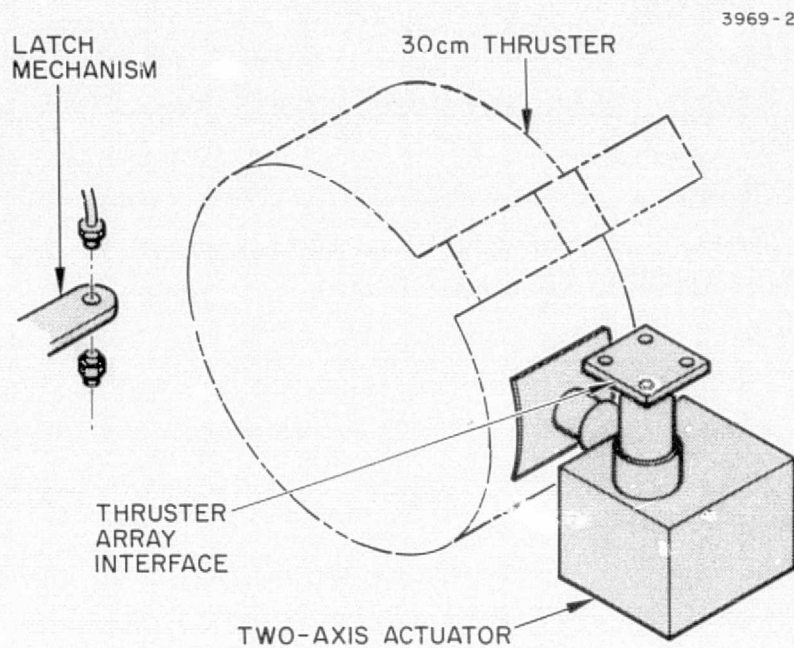


Figure 33. JPL gimbal concept.

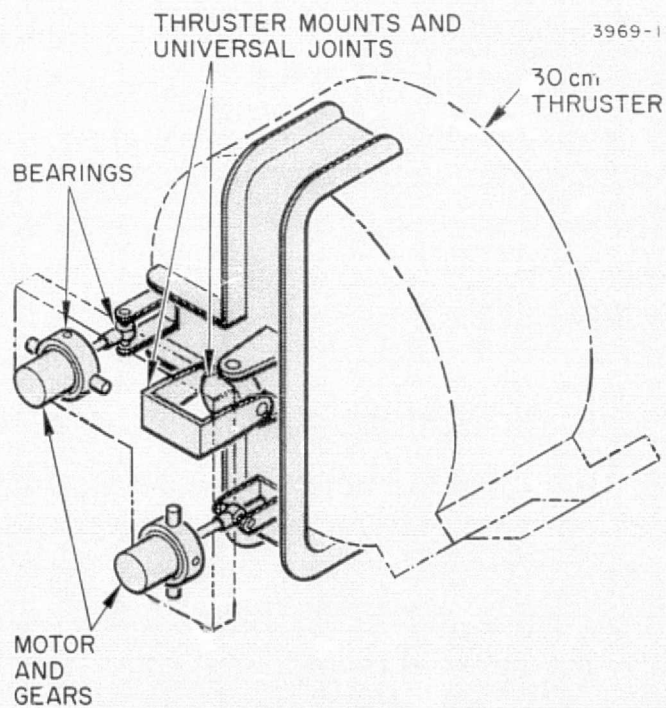


Figure 34. Rockwell linear actuator gimbal concept.

these designs reflect approaches in which thruster thermal control is not required. However, both approaches provide insulation between the thrusters and vehicle body.

Both Rockwell and Boeing selected thruster two axis gimbaling concepts. The Rockwell concept, similar to that shown in Fig. 34 uses linear actuators of the type developed at JPL for midcourse rocket engine gimbaling. The Boeing concept, shown in Fig. 35, uses motor driven tape type actuators to rotate the thruster around the thrust axis and around the thruster gimbal axis. The tape drive approach potentially provides simplicity and low backlash, but may require shielding from direct solar radiation.

A comparison of the failure rates and weights for these three systems as well as the more conventional tape driven mechanism (Fig. 36) has been made by breaking the systems up into similar components as shown in Table IX. By using consistent failure rates for similar components, the comparison should be valid even though each system uses different gimbaling techniques. On the basis of the similarity in failure rates seen here, selection of a gimbal mechanism on the basis of reliability is not considered possible, however the lower weights for the Boeing design and the conventional tape drive mechanism favors the latter two designs. The weights shown in Table IX are for a single thruster and were estimated using consistent weights for similar components.

#### B. Thruster Gimbaling Computer Program

A necessary step in the general area of gimbal requirement definition and gimbal approach selection is the generation of parametric trade study data. In order to select a given thruster array pattern and gimbal angle, one must have the means for computing torques about three axes, the maximum or net gimbal, and thrust losses. In addition, the gimbal angle needed to achieve a given torque level will place constraints on thruster-to-thruster positioning. Thruster positioning in turn will affect torque capability, making the selection of a gimbal angle and thruster pattern an iterative process. To facilitate this

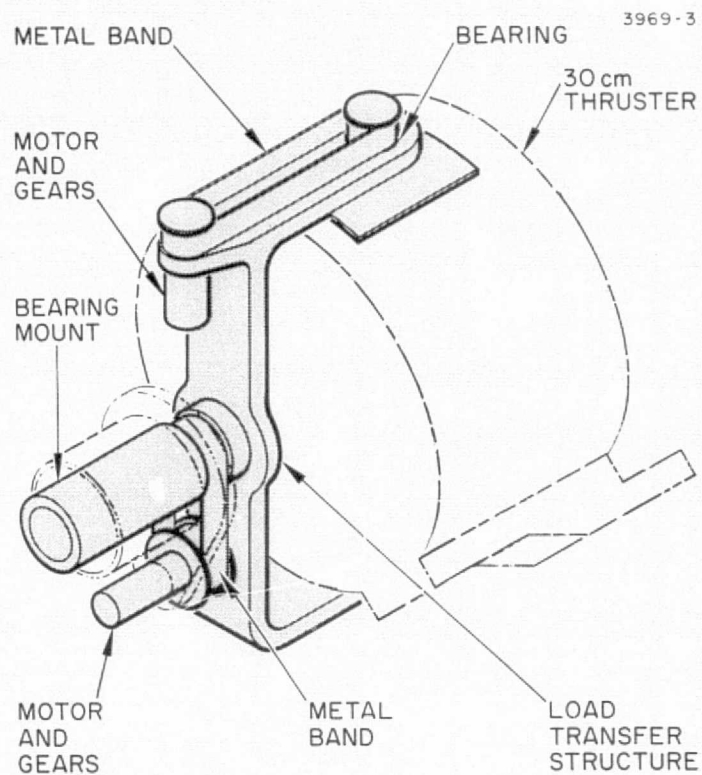


Figure 35. Boeing tape drive gimbal concept.

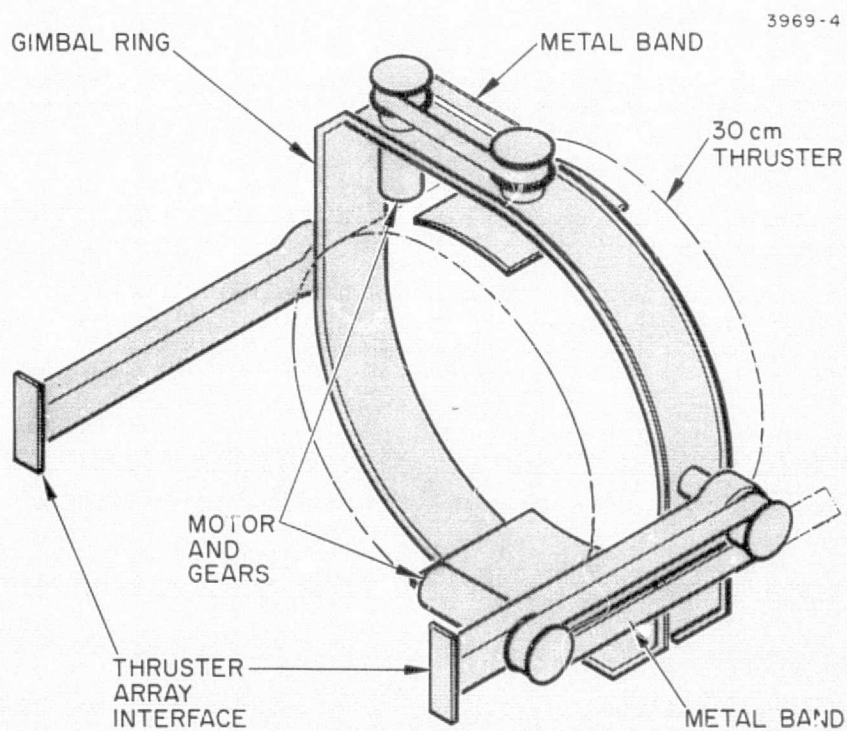


Figure 36. Conventional tape drive gimbal concept.

Table IX. Summary of Estimated Failure Rates (failures/ $10^6$  hr) and Weights for Different Thruster Gimbal Systems

Component	JPL Two Axis Activation	Boeing Tape Drive	Rockwell Linear Actuator	Conventional Tape Drive
Stepper Motors	0.22	0.22	0.22	0.22
Bearings, Main	0.11	0.11	0.11	0.11
Shaft, Stub	0.16	0.08	—	0.48
Shaft, Main Mount	—	0.14	0.28	—
Potentiometers	0.25	0.25	0.25	0.25
Metal Tapes	0.18	0.18	—	—
Pulleys	0.14	0.14	—	—
Ball Screws	—	—	0.07	0.07
Rod Ends, Bearing	—	—	—	0.02
Bearings, Motor Gimbal	—	—	—	0.22
Gear Sets	0.018	0.018	0.018	0.018
Bearings, Gear	0.008	0.008	0.008	0.008
Shaft Seal	—	—	0.03	—
Gasket	—	—	0.01	—
Bell Cranks	—	—	0.17	—
Leaf Spring Links	—	—	0.20	—
Total Failure Rate	1.09	1.15	1.37	1.40
Estimated weight (Kg)	3.26	2.35	3.9	2.4

T1875

process a computer program was written to calculate thrust, total gimbal angle for each thruster, net thrust including gimbaling, thrust vector direction, and torques about three orthogonal axes as a function of the following parameters:

Number of operating thrusters

Thruster pattern

Vehicle center-of-mass location

Gimbal angles ( $\alpha$  and  $\beta$ ) for each thruster

Gimbaling strategy (i.e., choice of which thrusters are to be used for roll, pitch, and yaw functions).

The computer program outputs are:

Total thrust loss

Resultant thrust vector

Resultant torques

Net gimbaling angle for each thruster.

### C. Analysis

#### 1. Forces

In vector rotation, the thrust vector of the  $i$ th thruster in the vehicle coordinate system is related to the thrust vector in the primed (thruster) coordinate system by  $\vec{F}_i = \lambda \vec{F}_i'$  where

$$F_i' = \begin{pmatrix} F_y' \\ F_z' \\ F_x' \end{pmatrix} \text{ and } F_i = \begin{pmatrix} f_y \\ f_z \\ f_x \end{pmatrix} \quad (7)$$

and  $\lambda$  is the matrix of direction cosines which represent two successive rotations by  $\alpha$  and  $\beta$ . For the case shown in Fig. 37, assuming rotation by angle  $\beta$  about this Y axis is applied first,  $\lambda$  is given by the product of matrices representing rotations about the x and y axis. Thus for a rotation by angle  $\beta$  about the Y axis the matrix is<sup>15</sup>

$$B = \begin{pmatrix} 1 & 0 & 0 \\ 0 & \cos\beta & \sin\beta \\ 0 & -\sin\beta & \cos\beta \end{pmatrix} \quad (8)$$

4977-12

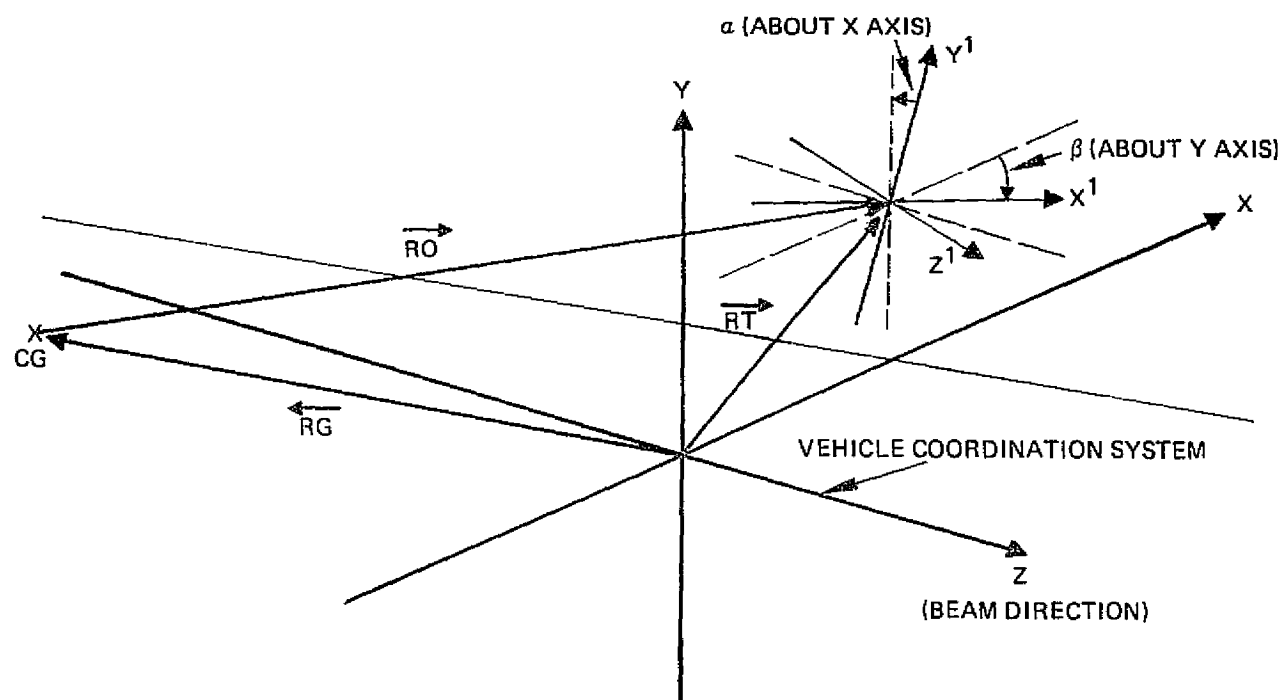


Figure 37. Coordinate system used for thrust and torque calculations. Each thruster has primed coordinate system with thrust in  $Z'$  direction and which is defined in unprimed coordinate by  $\vec{RT}$  vector and gimbal angles  $\alpha$  and  $\beta$  about  $x$  and  $y$  axis.



and for a rotation by angle  $\phi$  about the x axis the matrix

$$A = \begin{pmatrix} \cos\alpha & \sin\alpha & 0 \\ -\sin\alpha & \cos\alpha & 0 \\ 0 & 0 & 1 \end{pmatrix} \quad (9)$$

The resultant matrix for two successive rotations assuming  $\beta$  is applied first is given by the product of these two matrices or

$$= AB = \begin{pmatrix} \cos\alpha & (\sin\alpha \cos\beta) & \sin\alpha \sin\beta \\ -\sin\alpha & (\cos\alpha \cos\beta) & \cos\alpha \sin\beta \\ 0 & -\sin\beta & \cos\beta \end{pmatrix} \quad (10)$$

Since there is only a Z component of force in the primed system eq. (7) can be written in component form in the vehicle coordinate system using eqs. (7) and (10) (for each thruster)

$$\begin{aligned} f_z &= (\cos\alpha) (\cos\beta) |f| \\ f_y &= (\sin\alpha) (\cos\beta) |f| \\ f_x &= (-\sin\beta) |f| \end{aligned} \quad (11)$$

The x and y gimbal angles  $\alpha$  and  $\beta$  combine to form a total gimbal angle  $\gamma$  given by

$$\gamma = \frac{f_z}{|f|} = \cos^{-1} (\cos\alpha \cos\beta) \quad (12)$$

where  $|f|$  is the magnitude of the total force for each thruster. The resultant total force for the thruster array is evaluated by summing eq. (11) for each thruster. That is, the total forces  $F_x$ ,  $F_y$ , and  $F_z$  are given by

$$\begin{aligned}
 F_x &= \sum_i f_x , \\
 F_y &= \sum_i f_y , \\
 F_z &= \sum_i f_z .
 \end{aligned}
 \tag{13}$$

The resultant thrust loss is

$$\text{Thrust loss} = \left( 1 - \frac{F_z}{\sum f_i} \right) 100 \cdot (\%) .
 \tag{14}$$

The resultant thrust vector makes angles A, B, and C with the x, y, and z axes of the vehicle coordinate system and can be calculated as follows:

$$\begin{aligned}
 A &= \cos^{-1} \frac{F_x}{F_T} \\
 B &= \cos^{-1} \frac{F_y}{F_T} \\
 C &= \cos^{-1} \frac{F_z}{F_T}
 \end{aligned}
 \tag{15}$$

where

$$F_T = \sqrt{F_x^2 + F_y^2 + F_z^2} .
 \tag{16}$$

## 2. Torques

In vector notation the torque about the vehicle CG due to an arbitrary thruster is given by (see Fig. 35)

$$\vec{T} = \vec{RO} \times \vec{F} \quad (17)$$

and

$$\vec{RO} = \vec{RT} - \vec{RG} . \quad (18)$$

So in component form, if a thruster has position components  $x_1$ ,  $y_1$ , and  $z_1$ , in the vehicle coordinate system and the CG has coordinates  $x_0$ ,  $y_0$ , and  $z_0$ , then using (18) the component for the  $\vec{RO}$  vector are given by

$$\begin{aligned} r_x &= x_1 - x_0 \\ r_y &= y_1 - y_0 \\ r_z &= z_1 - z_0 \end{aligned} \quad (19)$$

So in component form the torques from an individual thruster are:

$$\begin{aligned} t_x &= r_y f_z - r_z f_y \\ t_y &= r_z f_x - r_x f_z \\ t_z &= r_x f_y - r_y f_x \end{aligned} \quad (20)$$

where  $f_x$ ,  $f_y$ , and  $f_z$  are given by eq. (11). The resultant total torques are evaluated by summing eq. (20) for the array.

### 3. Computer Program

A Fortran IV computer program was written to solve the above torque and force equations. The program was developed on the DEC-system 10 time sharing system and should run on other computer systems with minor coding changes. A complete program source listing is shown in Appendix A. To illustrate the use of this program we will solve for the resultant torques, forces etc., for a 3 x 3 thruster array with seven operating thrusters. For this configuration the two corner pairs and an inner pair are gimballed to produce the maximum roll torque subject to the constraint of a maximum total gimbal angle of  $28^\circ$  for any gimballed thruster. These thrusters are mounted on a 27 in. (0.636 m) square pattern and the vehicle CG is symmetrically placed 56 in. (1.422 m) to the rear of the thrusters mounting plate. The computer print-out for this configuration is shown in Fig. 38. The program first prints out the input data which include the thruster and CG coordinate and the gimbal angles. The output data includes the thrust and torque components for each thruster along with the total gimbal angles and a summary of resultant torques and forces and the total thrust loss.

```

      7 THRUSTERS:  CG AT X= 0.00M  Y= 0.00M  Z=-1.42
THRUSTER  X(M)    Y(M)    Z(A)    ALP(DEG)  BET(DEG)  THRUST(MLBS)
1         0.69    0.69    0.00    20.0      20.0      30.0
2        -0.69    0.69    0.00   -20.0      20.0      30.0
3        -0.69    0.00    0.00    28.0       0.0      30.0
4         0.00    0.00    0.00     0.0       0.0      30.0
5         0.69    0.00    0.00    28.0       0.0      30.0
6         0.69   -0.69    0.00    20.0     -20.0      30.0
7        -0.69   -0.69    0.00   -20.0     -20.0      30.0
-----
THRUSTER   FX      FY      FZ      TX      TY      TZ      THETA
1        -10.26    9.64   26.49    .015   -.107   .045   27.99
2        -10.26   -9.64   26.49   .105   .012   .045   27.99
3         0.00   14.08   26.49   -.066   .060  -.032   28.00
4         0.00    0.00   30.00    .000    .000   .000    0.00
5         0.00   14.08   26.49   -.066   -.060   .032   28.00
6         10.26    9.64   26.49   -.105   -.012   .045   27.99
7         10.26   -9.64   26.49   -.015   .107   .045   27.99
-----
TOTAL:      0.00   28.17 138.94  -0.131  -0.000   0.179
THRUST LOSS= 10.03% A= 90.00deg B= 81.52deg G= 8.48deg

```

Figure 38. Computer printout for thruster gimbaling computer program.

## VI. CONCLUSIONS

The work performed under this 2.5 kW Advanced Technology Ion Thruster Program provided a quantitative assessment of the performance capabilities and limitations of the 700/800 series Engineering Model Ion Thruster. Measurements made over a range of thruster control parameters show that the total thruster efficiency is not changed significantly by parameter selection if the data is corrected to account for thrust losses from doubly-charged ions and beam divergence. Performance data were obtained for variations of beam current (throttling) from 0.5 A to 2.75 A and the corrected thruster efficiency is in good agreement with that predicted using Kaufman's maximum propellant utilization theory. Equilibrium temperatures of thruster components were well within the limits considered satisfactory except at the lowest beam current levels where some isolator heater power is required to prevent propellant condensation.

Double ionization is a major problem area and places limitations on both the thruster efficiency and the discharge chamber lifetime. Data obtained under this program show a definite relationship between doubly-charged ion production and propellant utilization efficiency (for a given thruster). The transmission of the ion optics accelerator grid is found to have the greatest effect on this proportionality and reduction in accelerator aperture diameter was the only method observed to be successful in significantly reducing double ionization. The capabilities and/or the disadvantages of this design modification were by no means exhaustively explored under this program, and many questions remain to be answered. Discharge voltage, discharge power and beam current also influence doubly-charged ion production, but to lesser degrees. High power operation obtained by increasing beam current using this thruster design will definitely reduce thruster lifetime because of increased double ionization.

Thruster/power conditioning interactions were explored and concluded to be more a question of the specific thruster and power supply combination than a general problem. Oscillations in discharge current and/or voltage are nearly always observed. These oscillations were not proven to be detrimental in any manner that affects thruster efficiency or overall thruster operability. Isolated incidents of troublesome operation have been observed, but in general, the power conditioning as defined under preceding programs (Contracts NAS 3-14140, NAS 3-16528, NAS 3-16949) can provide satisfactory operation and control for the 700-800 series Engineering Model Thruster over a wide operating range. Several options for using the discharge power supply to provide the functions of other separate power supplies were demonstrated and consequently the power conditioning could be made lighter and more reliable by eliminating these separate power supplies. Similarly, it was demonstrated that the accelerator supply could be incorporated in the screen (beam) power supply.

A study of gimbal actuator requirements showed that a "universal" actuator design is not feasible because of the relatively wide range of requirements that can be identified with specific applications. A computer program was developed to aid in analyzing gimbal actuator requirements in place of attempting to design a general purpose actuator.

## REFERENCES

1. R. L. Poeschel, H. J. King, and D. E. Schnelker, "An Engineering Model 30 CM Thruster," AIAA Paper No. 73-1084, Lake Tahoe, Nev. (1973).
2. J. S. Sovey and H. J. King, "Status of 30 CM Mercury Ion Thruster Development" AIAA Paper No. 74-1117, San Diego, Calif. (1974).
3. H. J. King, et al., "Low Voltage 30 CM Ion Thruster Development," NASA CR-134731, October 1974.
4. B. G. Herron, J. D. Worden, and J. M. Simpkins, "A 30 CM Thruster Power Processor Test Console," AIAA Paper No. 73-1104, October 1973.
5. B. Banks, V. Rawlin, A. Weigand, and J. Walker, "Direct Thrust Measurement of a 30 cm Ion Thruster."
6. H. R. Kaufman, "Ion-Thruster Propellant Utilization," J. Spacecraft and Rockets 9, No. 7, July 1972, pp. 511-517.
7. F. F. Terdan and R. T. Bechtel, "Control of a 30 CM Diameter Mercury Bombardment Thruster," AIAA Paper No. 73-1079, Lake Tahoe, Nev. (1973).
8. HRL Technical Staff, "2.5 kW Advanced Technology Ion Thruster," NASA CR-134687, August 1974.
9. R. P. Vahrenkamp, "Measurement of Double Charged Ions in the Beam of a 30 cm Mercury Bombardment Thruster," AIAA Paper 73-1057, Lake Tahoe, Nevada, October 1973.
10. C. Collett, "A 7700 Hour Endurance Test of a 30 CM Kaufman Thruster," AIAA Paper No. 75-366, New Orleans, La., March 1975.
11. T. D. Masek, "Plasma Properties and Performance of Mercury Ion Thrusters," AIAA Paper 69-256, March 1969.
12. G. S. Perkins, et al., "A Mechanism for Three-Axis Control of an Ion Thruster Array," AIAA Paper 70-1156, AIAA 8th Electric Propulsion Conference, Stanford, California, August, 1970.
13. J. H. Duxbury, and J. H. Gerpheide, "Solar Electric Propulsion Encke Slow-Flyby 1979 Mission and Spacecraft Description," JPL Report 701-200, June 28, 1974.

14. "Concept Definition and Systems Analysis Study for a Solar Electric Propulsion Stage," Rockwell International Final Report on NAS 8-30920, SD 74-SA-0176, February 1975.
15. "Concept Definition and Systems Analysis Study for a Solar Electric Propulsion Stage," Boeing Aerospace Company Final Report on NAS 8-30921, D180-18553, January, 1975.
16. H. Goldstein, "Classical Mechanics," Addison and Wesley, 1959, p. 126.



## APPENDIX

### SOURCE LISTING FOR THRUSTER GIMBALLING COMPUTER PROGRAM

A source program listing for the thruster gimballing computer program is shown below. The input data for the thruster and CG coordinates are in meters, the forces are in mlbs and the gimbal angles are in degrees. The program outputs are given in lb-ft for the torques and mlbs for the forces.

```

        DIMENSION XX(20), YY(20), ZZ(20), AA(20), BB(20), CC(20),
        TH(20) OPEN(UNIT=20, FILE='DATA.DAT')
C   READ # OF CASES, # OF THRUSTERS, AND CG COORDINATES
    (IN METERS)
        READ(20, *) NCASE, NTHRUS, X, YO, ZO
        WRITE(5, 100) NTHRUS, XO, YO, ZO
        C1=3.14159/180.
        C2=.00328084
        DO 20 JXX=1, NCASE
C   C2 CONVERTS MLBS*M TO LB*FT
        WRITE(5, 200)
        DO 10 I=1, NTHRUS
C   READ THRUSTER COORD., GIMBAL ANGLES, AND THRUST
    (M, DEG, AND MLBS)
        READ(20, *) XX(I), YY(I), ZZ(I), AA(I), BB(I), TH(I)
10    WRITE(5, 300) (, XX(I), YY(I), ZZ(I), AA(I), BB(I), TH(I)
C   INITIALIZE SUMS
        TT=0.
        FXX=0.
        FYY=0.
        FZZ=0.
        TXX=0.
        TYY=0.
        TZZ=0.
        WRITE(5, 310)
        WRITE(5, 550)
        DO 6 I=1, NTHRUS
            X=XX(I)
            Y=YY(I)
            Z=ZZ(I)
            A1=AA(I)
            B1=BB(I)
            T=TH(I)
            TT=TT+T
    
```

```

C   CAL GIMBAL ANGLES IN RADIANS
      A=C1*A1
      B=C1*B1
C   COMPUTE COMPONENTS OF VECTOR BETWEEN CG AND
    THRUSTER
      RX=(X-XO)*C2
      RY=(Y-YO)*C2
      RZ=(Z-ZO)*C2
C   COMPUTE FORCE COMPONENTS IN S/C COORD. SYSTEM
      FX=-SIN(B)*T
      FY=SIN(A)*COS(B)*T
      FZ=COS(A)*COS(B)*T
C   COMPUTE TORQUES ABOUT CG
      TX=RY*FZ-RZ*FY
      TY=RZ*FX-RX*FZ
      TZ=RX*FY-RY*FX
C   ADD UP TORQUES AND FORCES
      TXX=TXX+TX
      TYY=TYY+TY
      TZZ=TZZ+TZ
      FXX=FXX+FX
      FYY=FYY+FY
      FZZ=FZZ+FZ
C   CALCULATE TOTAL GIMBAL ANGLE FOR EACH THRUSTER
    (IN DEG)
      TOT=ACOS(COS(A)*COS(B))/C1
6    WRITE(5,400) I,FX,FY,FZ,TX,TY,TZ,TOT
      FTOT=SQRT(FXX+FXX+FYY*FYY+FZZ*FZZ)
      THETAX=ACOS(FXX/FTOT)/C1
      THETAZ=ACOS(FZZ/FTOT)/C1
      THETAY=ACOS(FYY/FTOT)/C1
      TLOSS=(1.-FZZ/TT)*100.
      WRITE(5,310)
      WRITE(5,500) FXX,FYY,FZZ,TXX,TYY,TZZ
      WRITE(5,350) TLOSS, THETAX,THETAY,THETAZ
20  CONTINUE
500  FORMAT(6X,'TOTAL: ',F6.2,2X,F6.2,1S,F6.2 &
      2X,F6.3,3X,F6.3,2X,F6.3)
500  FORMAT(6X,'THRUSTER FX  FY  FZ
      & .TX  TY  TZ  THETA')
100  FORMAT(12X,13,'THRUSTERS: CG AT X=',F5.2,'M Y=',
      & F5.2,'M z=',F5.2)
200  FORMAT(1H-,6X,'THRUSTER (X(M) Y(M) Z(M) ALP(DEG)
      BET(DEG) & THRUST(MLBS)')
310  FORMAT(15X,'-----')
300  FORMAT(6X,13,6X,F5.2,3X,F5.2,2X,F5.2,3X,F5.1,
      4X,F5.1,8X,F5.1)
400  FORMAT(6X,13,5X,F6.2,2X,F6.2,2X,F5.2,3X,F5.3,
      4X,F5.3,3X,&F5.3,3X,F6.2)
350  FORMAT(1X,'THRUST LOSS=',F6.2,'% A=',F6.2,'deg
      & B=',F6.2,'deg G=',F6.2,'deg')
      END

```